This manuscript is a non-peer-reviewed preprint submitted to EarthArXiv.

A Transformer-Based Surrogate for Distributed Groundwater Dynamics with Zero-Shot Cross-Basin Transfer and Precipitation-Regime Data Augmentation

Hui Huang[1], Aoqi Sun[1], Hoang Tran[2], Yongjiu Dai[1], Chen Yang[1*]

[1]School of Atmospheric Sciences, Sun Yat-sen University, Zhuhai, China
[2]Atmospheric Science & Global Change Division, Pacific Northwest National Laboratory, Richland, WA, USA

*Correspondence to: Chen Yang (yangch329@mail.sysu.edu.cn)

Key Points:

- A groundwater-adapted PredFormer surrogate captures regional water-table dynamics.
- Zero-shot transfer achieved errors comparable to the source basin without target-basin training or fine-tuning.
- Precipitation-regime augmentation was most effective when added samples matched the prediction conditions.

Abstract

Large-scale physically based groundwater models generate spatially distributed simulations, but their cost limits the regional datasets available for training artificial-intelligence-based surrogates. Here, we developed and systematically evaluated a groundwater-adapted PredFormer surrogate for regional ParFlow-CLM simulations. The framework uses temporal-first factorized attention, pressure-residual prediction, prescribed precipitation-minus-evapotranspiration (PME) forcing, and static hydrogeological attributes. The model was developed and evaluated over the 34,000 km² upper Beijiang River basin (UBRB), with zero-shot transfer tested over the 24,000 km² Hejiang basin. Across 12 independent 720 h test segments, PredFormer maintained decimeter-scale water-table-depth errors. Upper-tail errors were associated with precipitation statistics, whereas abrupt wet–dry transitions coincided with temporal error fluctuations. PME reduced the overall mean absolute error from 0.151 to 0.099 m. Depth-stratified analysis showed that PME was most beneficial in shallow-water-table areas, whereas static attributes contributed most at intermediate depths and little in deep areas. PredRNN was more accurate initially, but PredFormer performed better at extended lead times, reducing the across-segment mean error at 720 h from 0.232 to 0.152 m. Without target-basin training, fine-tuning, or recalculation of standardization statistics, zero-shot transfer produced an overall mean error of 0.106 m in Hejiang, close to 0.099 m in the UBRB. Precipitation-regime data augmentation produced modest overall changes but clearer benefits when added samples matched prediction conditions; in a precipitation-active segment, the mean error decreased from 0.141 to 0.095 m. Together, these results show how groundwater state, training-data coverage, and cross-basin transfer shape the performance of Transformer-based groundwater surrogates.

Keywords: Transformer; groundwater surrogate modeling; precipitation-regime data augmentation; zero-shot cross-basin transfer; ParFlow-CLM

Plain Language Summary

Regional groundwater models can describe how water-table conditions change across large areas, but running these models requires substantial computing resources. We adapted PredFormer, a Transformer originally developed for video prediction, to create a fast surrogate model for regional groundwater dynamics. Transformers can learn how patterns at different locations and times are related, making them potentially useful for spatially distributed groundwater prediction. The model was developed and evaluated in the approximately 34,000 km² upper Beijiang River basin and used to predict water-table conditions continuously for 30 days. Precipitation and evapotranspiration information was particularly useful for predicting shallow groundwater, whereas fixed subsurface properties were more helpful at intermediate depths. Without additional training or adjustment using data from the target basin, the model achieved similar overall accuracy in the neighboring 24,000 km² Hejiang basin. Adding simulations representing different precipitation conditions was most beneficial when the added data matched the conditions encountered during prediction. These results demonstrate the potential of Transformer-based models for efficient regional groundwater prediction and clarify how environmental information and training-data coverage affect their performance.

1. Introduction

Over the past several decades, continuous improvements in numerical weather prediction systems, data assimilation techniques, and global observation networks have produced massive, spatiotemporally consistent datasets (Bauer et al., 2015), such as ERA5 and other global reanalysis products (Hersbach et al., 2020). The long-term accumulation of these high-quality numerical and observational datasets (X. Sun et al., 2025) has provided abundant training data spanning diverse meteorological conditions, substantially accelerating the adoption of artificial intelligence in weather and climate prediction and enabling the development of increasingly powerful data-driven models (Bi et al., 2023; Kochkov et al., 2024). More recently, these developments have progressed toward Earth foundation models (Bodnar et al., 2025; Nguyen et al., 2023) trained on heterogeneous Earth system datasets, marking a new stage in AI-driven Earth system modeling (Reichstein et al., 2019).

In comparison, groundwater modeling has historically been constrained by limited observations of subsurface hydraulic properties and groundwater states (Condon et al., 2021), making large-scale data-driven learning considerably more challenging (Jesse et al., 2025). Nevertheless, increasing recognition of groundwater as an active component of the Earth system (Reed M. Maxwell & Condon, 2016) has led to substantial developments in continental- and global-scale integrated hydrological models during the past two decades (Yang, Sun, et al., 2026). Physically based models, such as ParFlow-CLM (Kollet & Maxwell, 2008) and other integrated groundwater-land surface modeling systems (Kuffour et al., 2020), have generated increasingly extensive spatiotemporal simulations of groundwater states, soil moisture, evapotranspiration, and surface water fluxes (R. M. Maxwell et al., 2015). Although these simulated datasets remain considerably smaller and less constrained than atmospheric reanalysis products, they nevertheless provide an emerging data source that enables the development of data-driven groundwater surrogate models (Bennett et al., 2024; Tran et al., 2021).

Recent groundwater surrogate studies have demonstrated the feasibility of learning numerical model behavior using deep learning techniques (Chen et al., 2021; Li et al., 2022; Reed M. Maxwell et al., 2021). Existing studies have primarily employed recurrent neural network (RNN)-based architectures, including LSTM (Hochreiter & Schmidhuber, 1997), ConvLSTM (Shi et al., 2015), and PredRNN (Wang et al., 2017), to emulate groundwater dynamics or accelerate physically based simulations (Dai et al., 2025; Tran et al., 2021). More broadly, recurrent architectures continue to dominate many data-driven hydrological applications because of their ability to model temporal dependencies (Liu et al., 2025). However, recent developments in artificial intelligence have increasingly shifted toward Transformer-based architectures (Vaswani et al., 2017), which have shown remarkable success across computer vision (Dosovitskiy et al., 2021), natural language processing (Devlin et al., 2019), and, more recently, Earth system modeling (Gao et al., 2022). Compared with recurrent models, Transformers provide a fundamentally different mechanism for capturing long-range dependencies through self-attention (Vaswani et al., 2017) rather than sequential state propagation. While Transformer-based models have begun to emerge in hydrological prediction (Rasiya Koya & Roy, 2024), recent benchmarking studies suggest that no single architecture consistently outperforms others across different hydrological tasks and datasets (Liu et al., 2025). For distributed groundwater surrogate modeling, where long-term memory (Cuthbert et al., 2019), strong spatial heterogeneity (Condon et al., 2021), and complex groundwater-land surface interactions coexist (Kollet & Maxwell, 2008; Reed M.

Maxwell & Condon, 2016), the applicability of Transformer architectures remains largely unexplored.

To realize the full potential of Transformer architectures for distributed groundwater surrogate modeling, several challenges must first be addressed. Groundwater systems involve heterogeneous information sources, including dynamic state variables (e.g., pressure head and precipitation–evapotranspiration fluxes) (Bennett et al., 2024) and static hydrogeological attributes (e.g., topography, land surface characteristics, and subsurface hydraulic properties) (Kuffour et al., 2020), which interact across multiple temporal and spatial scales (Li et al., 2022). Effectively integrating these heterogeneous dynamic and static variables (Liesch & Ohmer, 2026) into a Transformer framework therefore becomes an important modeling question, as does understanding how their contributions vary across groundwater conditions (Heudorfer et al., 2024), including shallow and deep water-table regions. Beyond performance within a single basin, an equally important question is whether a surrogate trained in one regional domain can retain useful predictive skill when transferred to another basin (do Lago et al., 2023), at least where the hydroclimatic and hydrogeological settings are broadly comparable (Ohmer & Liesch, 2026). Although cross-basin transfer has received increasing attention in data-driven surface-water hydrology (Heidari & Khan, 2026; Kratzert et al., 2019), it remains largely unexplored in groundwater applications, where even the development of surrogates using physically based simulations of real-world regional basins remains limited (Asher et al., 2015). Finally, similar to recent developments in foundation models, improving model robustness under rare or underrepresented hydrometeorological conditions may require broader coverage of such conditions in the training data (Leonarduzzi et al., 2022; Xie et al., 2021), in addition to architectural advances (Leonarduzzi et al., 2022).

Motivated by these challenges, this study developed and systematically evaluated a Transformer-based surrogate for distributed groundwater dynamics by adapting PredFormer (Tang et al., 2026) to regional ParFlow-CLM simulations. Specifically, we address four scientific questions. First, can a Transformer-based surrogate accurately reproduce long-horizon groundwater dynamics during autoregressive prediction? Second, how should dynamic hydrological variables and static hydrogeological information be integrated within the Transformer framework, and how do their contributions vary across different groundwater conditions? Third, can a surrogate trained in one regional basin retain useful predictive skill under zero-shot transfer to another basin without target-basin training or fine-tuning? Fourth, can physics-based data augmentation, generated by perturbing precipitation forcing and rerunning the numerical model, improve model robustness under rare or underrepresented hydrometeorological conditions? Rather than seeking to demonstrate that Transformers universally outperform recurrent models, our objective is to identify the strengths and limitations of the adapted architecture across different groundwater and hydrometeorological conditions and to provide practical guidance for robust and transferable AI-driven groundwater modeling.

2. Study Areas and ParFlow-CLM Simulation Data

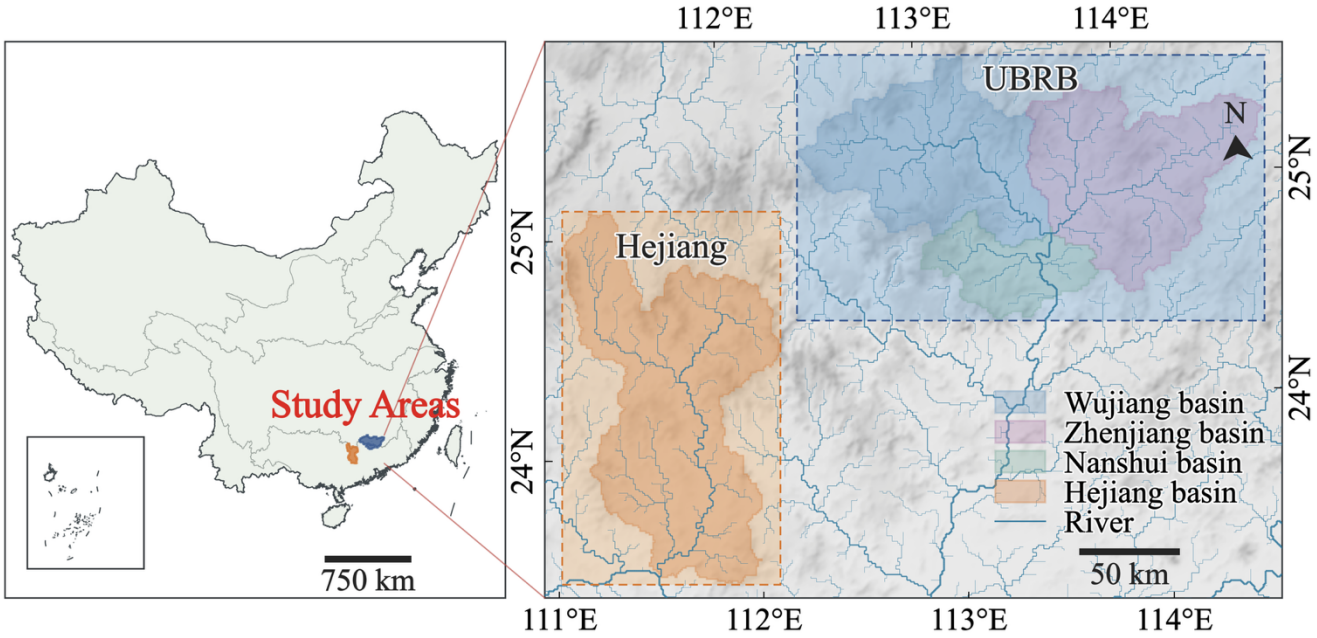


Figure 1. Study areas and regional ParFlow-CLM simulation domains. The study includes the upper Beijiang River basin (UBRB) and the neighboring Hejiang basin in the Pearl River basin, southern China. The UBRB comprises the Wujiang, Zhenjiang, and Nanshui River subbasins. The left panel shows the location of the study areas within China, whereas the right panel delineates the two simulation domains and the associated river network.

This study used two regional ParFlow-CLM simulation domains in southern China: the upper Beijiang River basin (UBRB) and the neighboring Hejiang basin (**Figure 1**). The UBRB domain covers approximately 34,000 km² and comprises the Wujiang, Zhenjiang, and Nanshui River subbasins, whereas the Hejiang domain spans approximately 24,000 km². The UBRB served as the source domain for surrogate-model development, systematic evaluation, and precipitation-regime data augmentation, while Hejiang served as the target domain for zero-shot cross-basin evaluation. The datasets used in this study were derived from hourly transient ParFlow-CLM simulations and the associated static model attributes for the two domains. The unperturbed UBRB simulations for WY2019–WY2021 (where WY denotes water year) were obtained from existing simulations conducted with the regional ParFlow-CLM model described by A. Sun et al. (2026). In this study, additional precipitation-perturbed UBRB simulations were conducted specifically for the data-augmentation experiments, and a separate regional ParFlow-CLM model of Hejiang was constructed and run for WY2021 to support the zero-shot evaluation. Further details of the zero-shot and data-augmentation experiments are provided in Sections 4 and 5, respectively.

ParFlow is an integrated hydrologic model that represents overland flow and three-dimensional variably saturated subsurface flow (Kollet & Maxwell, 2006). During the coupling, ParFlow provides soil-moisture and pressure-head (Press.) states to CLM, whereas CLM calculates the land-surface water and energy balances and returns the resulting layer-resolved P−ET (PME) fluxes to ParFlow as source–sink forcing through the upper four coupled subsurface layers (Reed M. Maxwell & Kollet, 2008; Reed M. Maxwell & Miller, 2005). The UBRB regional ParFlow configuration was extracted from CONCN

1.0 (Yang et al., 2025) and retained its model structure and parameterization, while the Hejiang configuration was constructed in this study following the same regional-model framework. Transient ParFlow-CLM simulations in both domains were driven by ERA5-Land meteorological forcing (Muñoz-Sabater et al., 2021). Detailed descriptions of CONCN 1.0 and the construction of the UBRB regional ParFlow-CLM model are provided by Yang et al. (2025) and Sun et al. (2026), respectively. Both domains used the same vertical discretization, comprising 10 subsurface layers with a total thickness of approximately 492 m. At a horizontal resolution of approximately 1 km, the UBRB domain contains 252 and 146 grid cells in the x and y directions, respectively, whereas the Hejiang domain contains 118 and 202 grid cells.

The dynamic fields obtained from the ParFlow-CLM simulations included pressure head, saturation, and the layer-resolved PME fluxes. In this study, the surrogate was developed specifically to emulate the groundwater dynamics represented by ParFlow, as a step toward its future hybrid coupling with a land-surface model. Explicit overland-flow states were therefore outside the scope of the present surrogate formulation. The surrogate was trained offline on precomputed ParFlow-CLM outputs rather than through interactive coupling to CLM. Within this formulation, the 10-layer pressure-head fields were used as both the dynamic state input and prediction target, while the four-channel PME fields associated with the four coupled subsurface layers were supplied as prescribed dynamic forcing. The static inputs comprised 31 channels representing the van Genuchten α and n parameters (van Genuchten, 1980), hydraulic conductivity, porosity, Manning's roughness coefficient, and surface slopes. The roles and channel numbers of these variables are summarized in **Table 1**. Saturation was retained as part of the ParFlow-CLM reference simulations but was not used as a surrogate input or prediction target. Water table depth (WTD) was diagnosed from the vertical pressure-head profiles and used for model evaluation.

Table 1. *ParFlow-CLM variables and parameters used in the groundwater surrogate model.*

Variable	Channels	Description
Pressure head	10	Groundwater pressure head used as the dynamic state input and prediction target of the surrogate model
PME	4	Layer-resolved net P−ET flux transferred from CLM to ParFlow as source–sink forcing (positive: source; negative: sink)
van Genuchten α	4	van Genuchten parameter related to the inverse of air-entry pressure head in the soil-water retention curve
van Genuchten n	4	van Genuchten parameter controlling the shape of the soil-water retention curve
Hydraulic conductivity	10	Hydraulic conductivity in the x direction
Porosity	10	Fraction of void space in the subsurface medium
Manning's coefficient	1	Manning's roughness coefficient for overland flow
Slope x	1	Surface slope in the x direction
Slope y	1	Surface slope in the y direction

3. Groundwater-Adapted PredFormer Framework

Transformer-based surrogates remain largely unexplored for distributed groundwater dynamics. To address this gap, we developed a groundwater-adapted PredFormer framework for distributed multilayer pressure-head prediction. The temporal-first factorized encoder was retained as the backbone, while the groundwater-specific adaptations included pressure-residual prediction, prescribed PME forcing, static hydrogeological conditioning, overlapping spatial-window reconstruction, and 12 h blockwise autoregressive rollout. Section 3.1 introduces the backbone architecture; Sections 3.2 and 3.3 describe the groundwater-specific prediction formulation and dynamic–static information fusion; Section 3.4 details model implementation and evaluation; and Section 3.5 defines the recurrent reference model. Additional architectural formulations are provided in Supplementary Information S1.

3.1 PredFormer as the Backbone Architecture

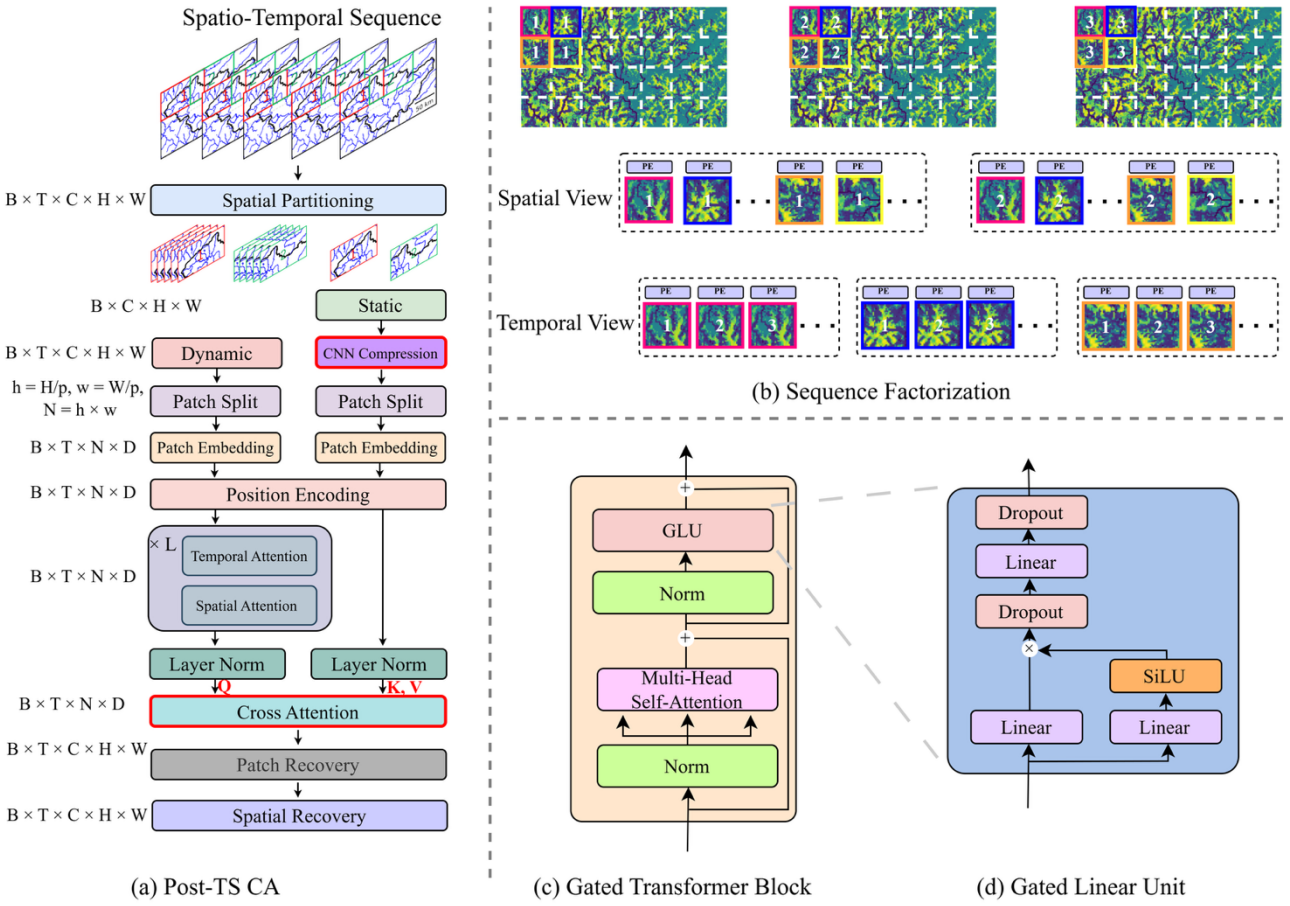


Figure 2. Groundwater-adapted PredFormer architecture. Panel (a) presents the overall framework. Dynamic pressure-head fields and prescribed PME are processed in overlapping spatial windows, divided into non-overlapping patches, and embedded as spatiotemporal tokens. Static attributes are compressed using a convolutional neural network (CNN) encoder and tokenized separately. The encoded dynamic tokens query the static tokens through post-temporal–spatial cross-attention, with dynamic tokens providing queries and static tokens providing keys and values. The model predicts pressure residuals relative to the final pressure state in the input sequence, and predictions from overlapping windows are averaged during spatial reconstruction. Panel (b) illustrates temporal-first factorized attention, panel (c) shows a Gated Transformer Block (GTB), and panel (d) shows the

SwiGLU (Shazeer, 2020) operation. PE denotes positional encoding; Q, K, and V denote queries, keys, and values, respectively.

PredFormer is a pure Transformer framework developed for spatiotemporal predictive learning, that is, predicting future states from observed spatiotemporal sequences (Tang et al., 2026). Its original applications represent video frames and other gridded fields as sequences of spatial tokens and learn their evolution over time. Groundwater dynamics exhibit a comparable spatiotemporal structure: distributed multilayer pressure-head fields contain complex spatial patterns, and these spatially distributed states evolve continuously through time. This correspondence motivated the use of PredFormer as the backbone of the ParFlow groundwater surrogate. Among the architectures evaluated in the original PredFormer study, the temporal-first factorized encoder (Fac-T-S) achieved the best performance on WeatherBench (Rasp et al., 2020), a gridded geoscience benchmark and the application most closely related to the present groundwater problem. We therefore adopted Fac-T-S as the starting configuration for modeling groundwater-state evolution.

Within each local spatial window, the pressure-head fields are divided into non-overlapping patches. Each patch is flattened and linearly projected into a token, after which spatiotemporal positional encoding is added to preserve its temporal and spatial location. The resulting token tensor has dimensions $B \times T \times N \times D$, where T and N denote the numbers of time steps and spatial patches, respectively. Temporal attention is first applied along the T tokens associated with each fixed spatial patch. The resulting representation is then rearranged, and spatial attention is applied across the N patches independently at each time step. This factorization reduces the attention complexity from $O(T^2N^2)$ for full spatiotemporal attention to $O(NT^2+TN^2)$, while retaining separate representations of temporal evolution and spatial interaction. The factorized encoder produces a spatiotemporal pressure-head representation and forms the PredFormer backbone used in this study. The final token representation is linearly projected back to the patch dimensions through patch recovery, and the recovered patches are reassembled to reconstruct the future pressure-head fields.

3.2 Residual Prediction and Autoregressive Rollout

Pressure head is a spatially coherent state field with strong temporal persistence (Cuthbert et al., 2019): each future field largely inherits the preceding state, while hydrological forcing and subsurface water redistribution produce incremental changes. A future pressure-head field can therefore be represented as the latest available state plus its subsequent change. Accordingly, rather than directly reconstructing absolute future fields as in the original PredFormer, the adapted model predicts pressure-head residuals relative to the latest available pressure-head state.

These residual predictions were incorporated into a blockwise autoregressive rollout. Let t_{start} denote the forecast initialization time of the current prediction block, corresponding to the final time step of its input block. The predicted pressure head at the i-th future time step was reconstructed as

$$\widehat{\text{Press.}}_{t_{\text{start}}+i} = \widehat{\text{Press.}}_{t_{\text{start}}} + \Delta\widehat{\text{Press.}}_{t_{\text{start}},\,i}, \quad i = 1, \ldots, L_{\text{out}},$$

where L_{out} denotes the number of forecast time steps in each output block, $\widehat{\text{Press.}}_{t_{\text{start}}}$ denotes the latest available pressure-head field at t_{start}, i.e., the final field of the current input block, and $\widehat{\Delta\text{Press.}}_{t_{\text{start}},\, i}$ denotes the predicted pressure-head residual at the *i*-th future time step. All residuals within a prediction block were defined relative to the same initial state and were not accumulated sequentially. Residual reconstruction was performed in standardized pressure space, after which the predicted pressure-head fields were transformed back to their original scale.

Both the input and output blocks consequently contained 12 hourly pressure-head fields. Each independent 720 h rollout was initialized once using the immediately preceding 12 h block of ParFlow-CLM reference pressure-head fields. This initial block was used to predict the first 12 h block, after which each predicted block was fed back as the input for the next prediction, without reintroducing reference pressure-head states. Repeating this procedure for 60 consecutive prediction blocks produced a continuous 720 h trajectory. During model development, we also tested a 24 h input–output configuration, but retained the 12 h configuration because it yielded better predictive performance.

3.3 Dynamic–Static Inputs and Fusion Strategies

Groundwater dynamics depend on the antecedent states of the groundwater system, temporally varying external forcing, and spatially heterogeneous hydrogeological and hydrogeomorphic conditions. The antecedent pressure-head sequence represents the prior evolution of the groundwater system, whereas PME provides dynamic source–sink forcing. Meanwhile, static attributes characterize the spatially varying subsurface and land-surface conditions that regulate the storage and transmission of water across the domain. For example, hydraulic conductivity affects subsurface water transmission, porosity influences water storage, and surface slopes define the topographic gradients driving overland flow (Kuffour et al., 2020), whereas Manning's roughness controls resistance to that flow. Therefore, dynamic forcing and static attributes may provide useful predictive information beyond antecedent pressure-head states.

We first investigated which types of information should be incorporated into the PredFormer backbone. Starting from a baseline using only pressure head (Press.), dynamic forcing and static attributes were progressively introduced, resulting in four input combinations: Press., Press. + PME, Press. + Static, and Press. + PME + Static. This experimental design was used to examine whether PME, static attributes, or their joint inclusion provided additional predictive information beyond the antecedent pressure-head sequence. To further examine the four input combinations across groundwater depths, the analysis was stratified by WTD into three zones: shallow (0–2 m), intermediate (2–20 m), and deep (>20 m).

We then considered how these additional inputs should be incorporated. Because the four-channel PME fields vary over time and are temporally aligned with the 10-channel pressure-head fields, they were directly concatenated with the pressure-head fields along the channel dimension before patch tokenization. The incorporation of static attributes required a more specific fusion design. The 31 static channels describe heterogeneous hydrogeological and hydrogeomorphic conditions and may exhibit

cross-channel redundancy. For example, hydrogeological properties may covary spatially with slope-related hydrogeomorphic information. We therefore compared four strategies for integrating static attributes into the dynamic representation.

The first strategy, Raw-Static Concatenation, repeated the original 31-channel static fields along the temporal dimension and directly concatenated them with the dynamic inputs before patch tokenization (**Figure S1a**). The second strategy, CNN-Compressed Static Concatenation, first compressed the 31 static channels into eight feature channels using a CNN encoder with a 3 × 3 convolutional kernel and then repeated and concatenated the compressed features with the dynamic inputs (**Figure S1b**). In addition to these concatenation-based strategies, we further considered cross-attention to integrate the static information into the evolving dynamic representation. Because this operation can be introduced at different stages of the PredFormer backbone, two configurations were evaluated. Pre-temporal–spatial (Pre-TS) Cross-Attention applied cross-attention before temporal-first factorized attention (**Figure S1c**), whereas Post-temporal–spatial (Post-TS) Cross-Attention applied it after temporal and spatial attention and before patch recovery and pressure prediction (**Figure 2**).

For cross-attention, let Z_d denote the dynamic-token representation at the selected fusion location and Z_s denote the CNN-compressed static-token representation. The fusion operation was formulated as

$$Q = \mathrm{LN}(Z_d), \quad K = V = \mathrm{LN}(Z_s),$$

$$Z_f = Z_d + \mathrm{CrossAttn}(Q, K, V),$$

where LN denotes layer normalization and Z_f denotes the fused representation. In the cross-attention operation, the normalized dynamic tokens serve as queries, whereas the normalized static tokens provide the keys and values. The query associated with each dynamic token is compared with the static keys to determine the attention weights assigned to different static tokens (Vaswani et al., 2017). The corresponding static values are then weighted and aggregated to produce a static-information update for that dynamic token. Because the cross-attention output retains the token organization and feature dimension of Z_d, it can be added back to the original dynamic representation through a residual connection. In this way, the evolving dynamic representation is conditioned on the static attributes while preserving the information already encoded in the dynamic tokens.

For the input-combination experiments, Post-TS Cross-Attention was used whenever static attributes were included. For the fusion-strategy experiments, all four strategies were evaluated using the complete Press. + PME + Static input combination. In both the Pre-TS and Post-TS Cross-Attention configurations, the 31-channel static attributes were first compressed into eight feature channels using the same CNN encoder architecture.

3.4 Model Implementation and Evaluation

Training samples were constructed through combined spatial and temporal sampling. Spatially, an additional windowing step was introduced before patch tokenization to adapt the PredFormer backbone to the full regional domain. The 252 × 146 grid was divided into overlapping spatial windows of 80 × 64 grid cells, with strides of 40 and 32 cells along the x and y directions, respectively. When the regular

stride did not reach the domain boundary, an additional boundary-aligned window was included along each spatial direction to ensure complete coverage. Each window was further divided into non-overlapping 8 × 8 patches, yielding a 10 × 8 grid of patches, or 80 spatial tokens, at each time step. Because adjacent windows overlapped, shared grid cells were represented using spatial context from more than one window. Window-level predictions were subsequently mapped back to the complete domain, and predictions for grid cells covered by multiple windows were reconstructed by arithmetic averaging. Temporally, samples were extracted using a stride of 6 h. For each spatial window, a sample contained 12 consecutive hourly pressure-head fields and a 12 h sequence of prescribed PME fields as dynamic inputs and was used to predict the subsequent 12 h pressure-head block. At each input-sequence position, the pressure-head state at time t was paired with the prescribed PME forcing at time t+1. For each sample, the static attributes were extracted from the same spatial window as the dynamic inputs and remained unchanged over time.

The ParFlow-CLM simulations from WY2019–WY2020 were used for model training, and the WY2021 simulation was used for testing. After the first 12 h of WY2021 were reserved to initialize the first forecast, the subsequent 8640 h were divided into 12 consecutive, non-overlapping segments of 720 h. For each segment, the immediately preceding 12 h pressure-head sequence was used to initialize the model. Each segment was initialized and evaluated independently, and prediction errors were not propagated across segment boundaries. All input and target variables were standardized before training. The mean and standard deviation used for standardization were calculated from the WY2019–WY2020 training data and applied to all training and test samples. Variables containing multiple vertical layers were standardized independently for each layer. The model was trained by minimizing the unweighted mean squared error between the predicted and ParFlow-CLM reference pressure-head fields in standardized space, averaged over all predicted elements in each training batch. All PredFormer configurations were trained for 60 epochs using the AdamW optimizer (Loshchilov & Hutter, 2019) with a batch size of 28 and an initial learning rate of 3×10^{-4}. A cosine learning-rate schedule (Loshchilov & Hutter, 2017) was applied throughout training. The checkpoint from the final training epoch was used to generate all test-set predictions.

WTD was calculated from both the predicted and ParFlow-CLM reference pressure-head fields. For segment i, forecast hour t, and grid cell k, the absolute WTD error was defined as

$$e_{i,t,k} = |\widehat{WTD}_{i,t,k} - WTD_{i,t,k}|.$$

Here, the hatted WTD term denotes the predicted value, and the unhatted WTD term denotes the ParFlow-CLM reference value. The spatial mean absolute WTD error, $E_{i,t}$, was obtained by averaging $e_{i,t,k}$ over all grid cells at each forecast hour:

$$E_{i,t} = \frac{1}{N_g}\sum_{k=1}^{N_g} e_{i,t,k},$$

where N_g is the number of grid cells. Let N_s and T denote the number of test segments and the number of forecast hours per segment, respectively (N_s = 12 and T = 720). The mean error at forecast hour t across all test segments, E_t, was calculated as

$$E_t = \frac{1}{N_s}\sum_{i=1}^{N_s} E_{i,t}.$$

The mean error over all forecast hours within segment i, E_i, was defined as

$$E_i = \frac{1}{T}\sum_{t=1}^{T} E_{i,t}.$$

The overall mean error across all segments and forecast hours, E, was therefore calculated as

$$E = \frac{1}{N_s}\sum_{i=1}^{N_s} E_i = \frac{1}{T}\sum_{t=1}^{T} E_t.$$

The hourly change in spatial mean absolute WTD error was calculated as

$$\Delta E_{i,t} = E_{i,t} - E_{i,t-1},\ t = 2, \ldots, T.$$

A positive value indicates an increase in spatial mean absolute WTD error between two consecutive forecast hours.

3.5 PredRNN as the Recurrent Reference Model

The recurrent reference model followed the groundwater surrogate implementation of Yang, Huang, et al. (2026), which was developed from PredRNN (Wang et al., 2023) and its groundwater-oriented adaptation by Bennett et al. (2024). The model advances the pressure-head field sequentially at hourly intervals using two stacked convolutional recurrent layers. Before prediction begins, the initial pressure-head field is encoded to initialize the shared memory state, while the static attributes are encoded to initialize the cell states of the recurrent layers. For each update from hour t to t+1, the pressure-head field at t and the prescribed PME field at t+1 are processed together with the recurrent states carried from the preceding update. The updated recurrent representation is projected to a pressure-head residual, which is added to the pressure-head field at t to reconstruct the field at t+1. In this study, the numbers of pressure-head and static-attribute channels were adjusted from 11 to 10 and from 32 to 31, respectively, while the remaining network architecture was retained from Yang, Huang, et al. (2026). This PredRNN configuration contained 76,784 trainable parameters, compared with 9.04 million for PredFormer. PredRNN therefore served as an established recurrent reference rather than a parameter-matched alternative to PredFormer.

For direct comparison, PredRNN was retrained using the same WY2019–WY2020 training period, prescribed PME forcing, static attributes, and 12 h target pressure-head sequences as PredFormer. Training sequences were sampled every 12 h from 16 × 16 subdomains extracted with a stride of 16 cells, with boundary-aligned windows added to ensure full-domain coverage. All variables were standardized using the channel-wise statistics calculated from WY2019–WY2020, identical to those used for PredFormer. For each training sample, PredRNN was initialized using the final pressure-head field from the preceding 12 h reference period and was then unrolled autoregressively over the 12 target hours. The training loss over the 12 predicted fields followed Yang, Huang, et al. (2026) and combined

the mean squared prediction error with a spatial-gradient loss weighted by 0.1 and a memory-decoupling loss weighted by 1.0. Optimization used AdamW for 80,000 iterations with a batch size of 28 and a weight decay of 0.01. A OneCycleLR (Smith & Topin, 2019) schedule used initial, maximum, and final learning rates of 4×10^{-4}, 2×10^{-3}, and 8×10^{-5}, respectively, and the final checkpoint was used for evaluation. For the WY2021 evaluation, both models predicted the same 12 independently initialized 720 h periods. PredFormer used the complete preceding 12 h pressure-head sequence for initialization, whereas PredRNN used only the final pressure-head field from that reference period. PredRNN then generated each 720 h prediction sequentially at hourly intervals.

4. Zero-Shot Cross-Basin Evaluation

To assess zero-shot cross-basin transfer, the same groundwater-adapted PredFormer used for the primary UBRB evaluation was applied directly to the Hejiang WY2021 simulation. The model used the complete Press. + PME + Static input combination and Post-TS Cross-Attention and had been trained exclusively on the unperturbed UBRB WY2019–WY2020 simulations. Its final-epoch checkpoint and the UBRB WY2019–WY2020 standardization statistics were retained, with no target-basin training, fine-tuning, or recalculation using Hejiang data. Following the procedure described in Section 3.4, the Hejiang WY2021 simulation was divided into the same 12 temporally aligned 720 h test segments used in the UBRB evaluation, with the same spatial windowing, full-domain reconstruction, and autoregressive rollout procedures. Predictions for each Hejiang segment were initialized with the preceding 12 h of Hejiang ParFlow-CLM reference pressure-head fields and generated using the prescribed Hejiang PME forcing and static attributes. The resulting spatial-mean absolute WTD error trajectories were compared with the corresponding UBRB test results. Precipitation conditions within each segment were summarized separately for each basin using the temporal mean and standard deviation of that basin's domain-mean hourly precipitation.

5. Precipitation Regimes and Data Augmentation

Extreme dry and wet conditions are often underrepresented in finite training records, which may limit a surrogate model's predictive ability when analogous conditions are encountered in prediction (Leonarduzzi et al., 2022; Xu et al., 2025). Physics-based simulations provide a practical means of generating additional, physically consistent examples beyond those contained in the unperturbed record. We therefore examined whether precipitation-regime-specific data augmentation, in which training samples representing selected precipitation conditions were added, could improve long-horizon groundwater prediction under the corresponding precipitation regimes.

Rather than directly perturbing pressure head or PME, which could disrupt the coupled relationships among precipitation forcing, water exchange between the land surface and subsurface, and groundwater states, we generated additional simulations by modifying the precipitation component of the ERA5-Land forcing. For WY2020 and WY2021, the precipitation forcing was multiplied by factors of 1.4 and 1.8, while all other meteorological forcings remained unchanged. ParFlow-CLM was then rerun for both perturbation scenarios, producing four additional simulation years in which pressure head, PME, saturation, and WTD remained physically consistent with the modified precipitation forcing.

Precipitation regimes were defined using the 24 h domain-mean accumulated precipitation, denoted as P_{24}. Each 24 h window was classified as Dry ($P_{24} < 1$ mm), Light ($1 \leq P_{24} < 10$ mm), Moderate ($10 \leq P_{24} < 25$ mm), or Heavy ($P_{24} \geq 25$ mm). Two windowing schemes were used for different purposes. Consecutive non-overlapping 24 h windows were used first to characterize hourly WTD responses in the unperturbed WY2019–WY2021 simulations and later to analyze WTD prediction errors, $\Delta E_{i,t}$, in the unperturbed WY2019 test simulation by precipitation regime. In contrast, overlapping 24 h windows with a temporal stride of 6 h were used to construct the surrogate-training samples and assign them to precipitation regimes for data augmentation. The same precipitation thresholds were applied to both windowing schemes.

Among the three unperturbed simulation years, WY2019 had the highest annual precipitation, with 1933.0 mm compared with 1509.3 mm in WY2020 and 1144.6 mm in WY2021. Accordingly, the augmentation experiments used a separate train–test split from the primary evaluation: the unperturbed WY2019 simulation was held out as the test period, whereas the unperturbed WY2020–WY2021 simulations formed the baseline training set. Additional training samples were drawn only from the precipitation-perturbed WY2020–WY2021 simulations; no samples from WY2019 were used for model training.

Four augmentation strategies were compared with the baseline training set (**Table 2**). All-1.4× added all 2916 candidate samples from the 1.4× precipitation simulations for WY2020–WY2021. Dry-1000 added 1000 Dry samples, ModHeavy-1000 added 1000 samples comprising 687 Moderate and 313 Heavy samples, and Heavy-all added all 313 available Heavy samples. For the Dry-1000, ModHeavy-1000, and Heavy-all strategies, samples were selected from the combined set of candidate samples generated by the 1.4× and 1.8× precipitation simulations for WY2020–WY2021. All configurations were evaluated using the same unperturbed WY2019 test period to determine whether augmenting selected precipitation regimes improved prediction under the corresponding precipitation conditions.

Table 2. Precipitation-regime composition of the additional training samples used in each augmentation strategy.

Strategy	Added samples				
	Total	Dry	Light	Moderate	Heavy
All-1.4×	2916	1311	1101	390	114
Dry-1000	1000	1000	0	0	0
ModHeavy-1000	1000	0	0	687	313
Heavy-all	313	0	0	0	313

6. Results and Discussion

6.1 Long-Horizon WTD Prediction and Error Evolution

Computational efficiency was evaluated using wall-clock runtime for a one-year simulation over the UBRB simulation domain. ParFlow-CLM was executed using 24 CPU cores on an AMD EPYC 9654 96-Core Processor, whereas PredFormer inference was performed using an NVIDIA A100-

SXM4-80GB GPU. Under these computational configurations, PredFormer required approximately 220 s, compared with about 2.5 h for ParFlow-CLM, corresponding to an approximately 41-fold speedup. The reported PredFormer runtime included data loading, preprocessing, and spatial reconstruction. To characterize long-horizon error propagation, **Figure 3** presents the spatial median of the absolute WTD error (referred to as the median error within this section) together with the spatial q25–q75 and q10–q90 ranges for all 12 test segments. A 720 h, or 30-day, horizon represents a practical timescale for examining groundwater evolution during prolonged wet and dry conditions relevant to drought and flood preparedness. Across the 12 segments, the median, q75, and q90 errors were initially small and generally increased with lead time. At 720 h, the final median error ranged from 0.071 to 0.140 m across segments.

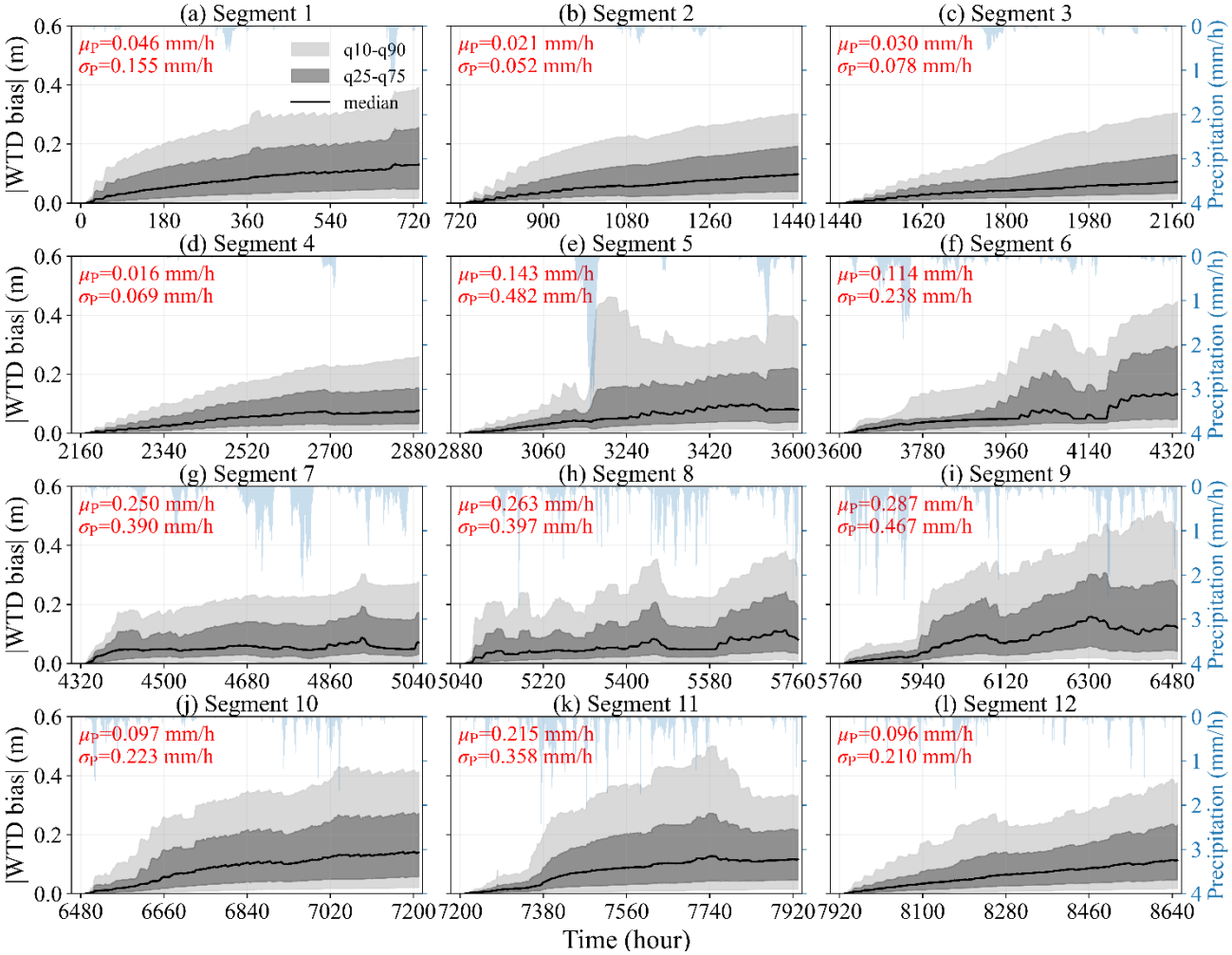


Figure 3. Segment-wise evolution of precipitation and WTD prediction error during 720 h autoregressive prediction. Panels (a–l) show the 12 independently initialized, non-overlapping 720 h segments from the independent WY2021 test simulation. Black curves show the spatial median of the absolute WTD error, dark and light shaded bands show the spatial q25–q75 and q10–q90 ranges, respectively, and blue bars show domain-mean hourly precipitation on the secondary *y*-axis. Red annotations report the mean (μ_P) and standard deviation (σ_P) of domain-mean hourly precipitation within each segment.

Across the 12 segments, two distinct aspects of error evolution were evident. First, the smoothness of the WTD error trajectories was generally associated with the temporal variability of precipitation (σ_P). Segments with relatively low σ_P, such as Segments 1–4, exhibited comparatively smooth and gradual error accumulation, whereas segments with more variable precipitation, including Segments 5–12, generally showed more pronounced fluctuations in their error trajectories. However, none of the final-hour median, q75, or q90 errors showed a clear monotonic relationship with either μ_P or σ_P (**Table 3**). Second, the most pronounced changes in error frequently coincided with abrupt transitions between relatively dry and wet conditions. In Segment 11, for example, the onset of substantial precipitation near simulation hour 7380 was accompanied by a sharp error increase, whereas the subsequent period of sustained precipitation produced a comparatively gradual increase. More strikingly, in Segment 9, the error remained relatively low during the initially wet period but increased markedly as precipitation weakened and conditions became drier. Similar event-associated error fluctuations were also visible in several other segments.

Table 3. Segment-level correlations between precipitation statistics and WTD prediction-error metrics (n = 12).

Precipitation metric	WTD error metric	Pearson r	Spearman ρ
Precipitation mean (μ_P)	720 h mean of spatial mean	0.462	0.476
	720 h mean of spatial median	0.247	0.287
	720 h mean of spatial q75	0.465	0.566
	720 h mean of spatial q90	**0.554**	**0.629**
	final-hour spatial mean	0.114	0.238
	final-hour spatial median	-0.023	0.105
	final-hour spatial q75	0.135	0.287
	final-hour spatial q90	0.192	0.378
Precipitation standard deviation (σ_P)	720 h mean of spatial mean	0.494	0.469
	720 h mean of spatial median	0.246	0.175
	720 h mean of spatial q75	0.467	0.469
	720 h mean of spatial q90	**0.600**	**0.608**
	final-hour spatial mean	0.203	0.231
	final-hour spatial median	-0.02	0.035
	final-hour spatial q75	0.233	0.259
	final-hour spatial q90	0.328	0.385

The segment-level correlation analysis further showed that the 720 h mean of the median error was only weakly associated with precipitation statistics (**Table 3**). Their strongest and most consistent relationships were observed for the 720 h mean of q90 error, with Spearman correlations of 0.629 for μ_P and 0.608 for σ_P. Thus, precipitation amount and temporal variability were associated primarily with the upper tail of the spatial error distribution rather than with a uniform increase in domain-wide or final-hour error. Together with the event-scale trajectories, these results suggest that larger grid-cell errors were more closely associated with segment-scale precipitation statistics, whereas fluctuations in the error trajectories coincided more closely with abrupt wet-dry transitions.

Figure 4 further illustrates how the spatial distribution of predicted WTD evolved during a representative segment (Segment 4). The adapted PredFormer reproduced the dominant spatial organization of the ParFlow-CLM reference WTD field and retained its broad spatial pattern as the rollout progressed. The signed differences were small at the beginning of the forecast but became progressively larger and more spatially heterogeneous with increasing lead time. Positive and negative differences were interspersed at relatively fine spatial scales, indicating that the prediction error did not develop as a spatially uniform offset. By 720 h, positive differences were more prevalent in the northwestern part of the domain, whereas negative differences were more prominent toward the southeast, revealing a broad spatial organization superimposed on the finer-scale error pattern. A complementary analysis across all 12 segments (**Table 4**) further stratified the absolute WTD errors according to the reference WTD. For the Press. + PME + Static configuration, the mean absolute errors, *E*, were 0.08913 m in the shallow zone (0–2 m), 0.02569 m in the intermediate zone (2–20 m), and 0.05682 m in the deep zone (>20 m). Thus, the errors were largest in shallow-groundwater areas, smallest at intermediate depths, and moderate in deep-groundwater areas.

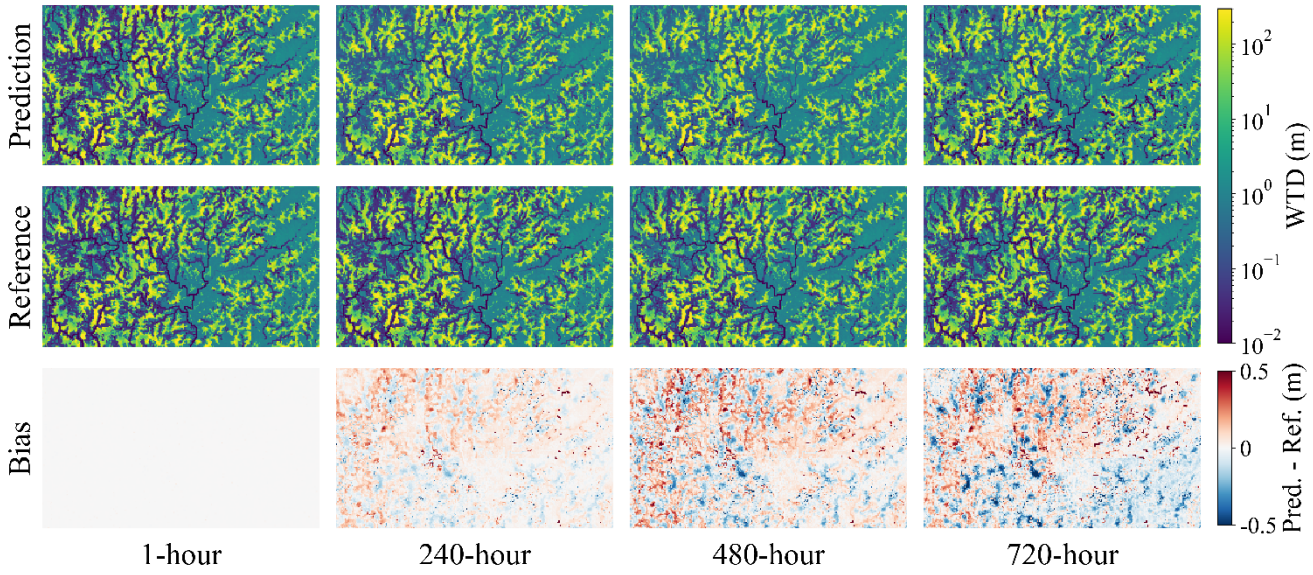


Figure 4. Spatial distributions of predicted and reference WTD and their differences at selected lead times during Segment 4. Segment 4 is taken from the independent WY2021 test simulation and spans hours 2172–2891. Columns show lead times of 1, 240, 480, and 720 h, corresponding to hours 2172, 2411, 2651, and 2891 of the WY2021 simulation, respectively. The first and second rows show the PredFormer predictions and corresponding ParFlow-CLM references, respectively. The bottom row shows the signed WTD prediction error, calculated as prediction minus reference. The first column represents the first predicted hour rather than the initialized state.

The adapted PredFormer provides a representation aligned with the spatiotemporal characteristics of distributed groundwater fields. Temporal-first attention relates pressure-state representations across the input sequence, spatial attention captures dependencies among spatial patches at each time step, and residual prediction expresses each output block as a change from the latest pressure state. Together, the results support the feasibility of the adapted PredFormer for long-horizon groundwater emulation, while also showing that its prediction errors remain sensitive to abrupt transitions between wet and dry

conditions. This remaining sensitivity highlights the importance of adequately representing such hydrological transitions in the training data.

6.2 Effects of Input Composition and Static-Attribute Fusion Strategies

The segment-wise results showed a broadly consistent pattern among the four input combinations (**Figure S2**). Adding static attributes to pressure head alone generally maintained or reduced the WTD error, although performance deteriorated in several segments, including Segments 6–9. Adding PME to pressure head produced a more consistent improvement, reducing the error across all 12 segments. In contrast, adding static attributes after PME had already been included did not provide a systematic additional benefit: the Press. + PME + Static configuration was comparable to or slightly worse than Press. + PME in most segments, although exceptions occurred, such as Segment 3, where the full input combination performed best. The across-segment mean error trajectory, E_t, summarized these patterns (**Figure 5a**): the overall mean error, E, decreased from 0.151 m for Press. alone to 0.138 m with static attributes and to 0.099 m with PME, while the full Press. + PME + Static configuration produced the same mean error of 0.099 m. Segment 11 provided a particularly clear example (**Figure 5b**), with segment-mean errors, E_i, of 0.301, 0.248, 0.117, and 0.125 m for Press., Press. + Static, Press. + PME, and Press. + PME + Static, respectively. These results indicate that PME provided the dominant and most consistent additional information, whereas the contribution of static attributes was smaller and depended on whether dynamic forcing had already been included.

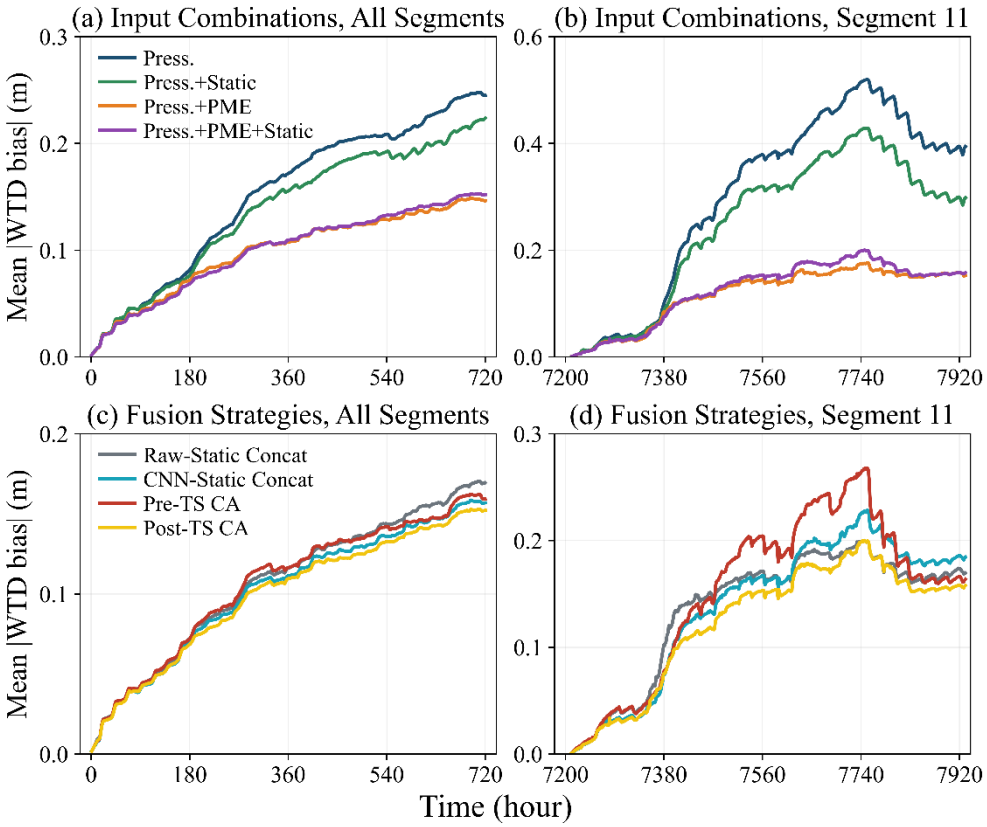


Figure 5. Effects of input composition and static-attribute fusion strategies on 720 h autoregressive WTD prediction in the independent WY2021 test simulation. Panel (a) shows the spatial-mean absolute WTD error averaged across the 12 segments for the four input combinations.

Panel (c) shows the corresponding comparison among the four static-attribute fusion strategies. Panels (b) and (d) show the input-combination and fusion-strategy results, respectively, for Segment 11.

The effects of the additional inputs varied systematically among the three WTD regimes (**Table 4**). In the shallow zone (0–2 m), adding PME to pressure head produced the largest improvement, reducing the overall mean error within this zone from 0.16472 to 0.07754 m, or by 52.93%. Adding static attributes alone produced a smaller reduction of 14.09%, while combining PME and static attributes resulted in an error of 0.08913 m. In the intermediate zone (2–20 m), static attributes provided the greatest improvement, reducing the error from 0.02395 to 0.02185 m, or by 8.77%, whereas the configurations containing PME produced slightly larger errors than Press. alone. In the deep zone (>20 m), Press. alone achieved the lowest error of 0.05623 m, and none of the additional-input configurations provided further improvement. These results reveal a depth-dependent shift in the information most useful for groundwater prediction: dynamic PME forcing was most informative for shallow groundwater, static attributes were more useful at intermediate depths, and the antecedent pressure-head state alone was sufficient for the deepest groundwater.

This depth dependence is consistent with the changing connection between groundwater and land-surface forcing (Kollet & Maxwell, 2008). Shallow water tables respond relatively directly to the upper-layer source–sink exchange represented by PME, making explicit information about the time-varying forcing particularly valuable. At intermediate depths, the surface-derived signal must propagate through a thicker unsaturated zone and is therefore attenuated and temporally smoothed. The magnitude and timing of the transmitted response become increasingly dependent on static hydraulic properties that regulate infiltration, storage, and vertical redistribution (Kuffour et al., 2020), helping explain the greater benefit of static attributes in this zone. For WTD greater than 20 m, the direct influence of land-surface forcing over the evaluated 720 h horizon is likely weaker, and groundwater evolution may be governed more strongly by antecedent subsurface conditions and slower lateral or regional groundwater flow (Cuthbert et al., 2019). Because the pressure-head sequence already contains the integrated effects of these prior conditions, adding PME or static attributes supplied little additional predictive information in the deep zone.

Table 4. Mean absolute WTD error averaged across all test segments and forecast hours for each WTD regime and input combination. Percentages in parentheses indicate changes relative to the pressure-head-only configuration within each regime.

WTD regimes	**Mean absolute WTD errors (m)**			
	Press.	**Press. + PME**	**Press. + Static**	**Press. + PME + Static**
Shallow (0–2 m)	0.16472	0.07754 (-52.93%)	0.14151 (-14.09%)	0.08913 (-45.89%)
Intermediate (2–20 m)	0.02395	0.02500 (+4.38%)	0.02185 (-8.77%)	0.02569 (+7.27%)
Deep (>20 m)	0.05623	0.05954 (+5.89%)	0.05936 (+5.57%)	0.05682 (+1.05%)

Compared with the choice of input variables, the static-fusion strategy produced relatively small differences in WTD prediction error (**Figure S3**). The four configurations showed broadly similar error trajectories across most segments, although their relative rankings varied from one segment to another. Some fusion configurations even slightly increased the error in particular segments. Nevertheless, Post-TS Cross-Attention showed the most consistent, although modest, advantage. Averaged across the 12

segments, the overall WTD errors, E, were 0.107 m for Raw-Static Concatenation, 0.102 m for CNN-Compressed Static Concatenation, 0.106 m for Pre-TS Cross-Attention, and 0.099 m for Post-TS Cross-Attention (**Figure 5c**). Thus, CNN compression alone produced a modest improvement over direct concatenation, and applying cross-attention after temporal–spatial encoding provided a further reduction in error. In contrast, introducing cross-attention before temporal–spatial encoding largely removed the benefit obtained through CNN compression. At a lead time of 720 h, Post-TS Cross-Attention reduced the error by 10.2% relative to Raw-Static Concatenation (**Figure 5c**). It also achieved the lowest mean error, E_i, in seven of the 12 segments (**Figure S3**). The distinction was particularly clear in Segment 11, where Post-TS Cross-Attention performed best and Pre-TS Cross-Attention produced the largest error (**Figure 5d**).

The modest improvement obtained through CNN compression suggests that the 31 static channels contained partly redundant or spatially covarying information and could be represented more effectively by a compact set of learned features. The additional advantage of Post-TS Cross-Attention may reflect a more effective separation between dynamic-state encoding and static conditioning. Post-TS Cross-Attention therefore first resolves temporal evolution and spatial interactions from the pressure-head and PME inputs and subsequently uses the compressed static attributes to condition the encoded dynamic representation before pressure reconstruction. By contrast, introducing static information before these temporal–spatial relationships have been resolved may partly duplicate information already embedded in the antecedent pressure state and thereby interfere with the encoding of subsequent dynamic evolution. This difference provides a plausible explanation for why Post-TS Cross-Attention produced a small but more consistent improvement, whereas Pre-TS Cross-Attention did not outperform CNN compression alone.

6.3 Comparison with a Recurrent Reference Model

Figure 6 shows that PredFormer and PredRNN exhibited distinct lead-time-dependent error behavior over the 720 h prediction horizon. PredRNN produced lower mean absolute WTD errors, E_t, during the early prediction period (**Figure 6a**), whereas PredFormer became more accurate after approximately 160 h, with the difference increasing at longer lead times. At 720 h, the across-segment mean absolute WTD error, $E_{t=720}$, was 0.152 m for PredFormer and 0.232 m for PredRNN. Averaged across all segments and lead times, the corresponding errors, E, were 0.099 and 0.136 m, respectively, and PredFormer achieved a lower segment-mean error, E_i, in 11 of the 12 test segments (**Figure S4**). Thus, the relative advantage of PredFormer emerged primarily over longer prediction horizons rather than during the initial prediction period. In addition to its lower long-horizon error, PredFormer exhibited a smoother error trajectory. This contrast was particularly evident in the precipitation-active Segment 9 (**Figure 6b**), where the PredRNN error showed pronounced temporal fluctuations, whereas the PredFormer error remained comparatively smooth. After calculating the temporal standard deviation of the spatial-mean absolute WTD error within each segment, the values averaged across the 12 segments were 0.082 m for PredRNN and 0.047 m for PredFormer, indicating that PredFormer produced less temporally variable error trajectories.

The contrasting error behavior may reflect differences in how the two models represent spatiotemporal dependencies and how frequently their predictions are fed back during autoregressive

rollout. PredRNN updates the pressure field sequentially at hourly intervals. Temporally, information is carried forward through recurrent states one hour at a time, whereas spatially, its convolutional operations exchange spatial information primarily within local neighborhoods. Long-range temporal dependencies must therefore be transmitted progressively through recurrent states, while long-range spatial interactions require stacked convolutional operations or repeated updates. Consequently, rapid changes in forcing are assimilated sequentially, while prediction errors can enter the recurrent memory at each hourly update and be repeatedly propagated, potentially producing larger fluctuations and error accumulation. PredFormer instead uses temporal attention across all input times for each spatial patch and spatial attention across all patches within a window, providing more direct pathways for representing long-range spatiotemporal dependencies. Moreover, its 12 h residual predictions are generated jointly relative to the final pressure state of the input block, so predicted states are fed back only once per 12 h block rather than at every hourly step. These differences provide a plausible explanation for the smoother error trajectories and greater long-horizon accuracy of PredFormer under the tested setting.

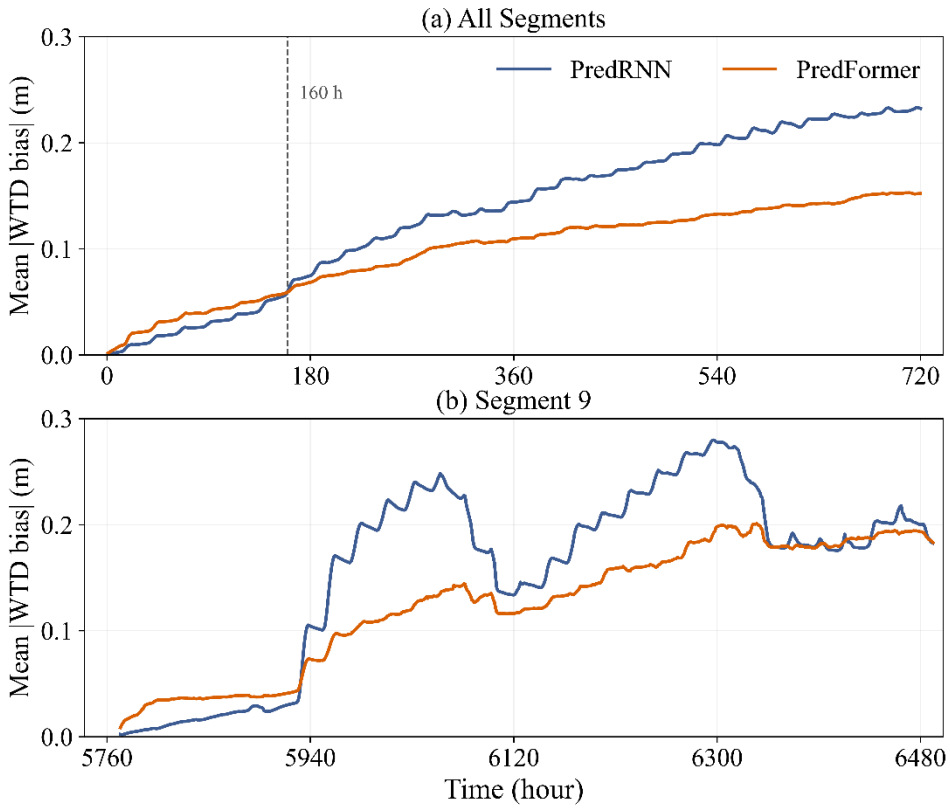


Figure 6. Long-horizon comparison between PredFormer and PredRNN. Panel (a) shows the spatial-mean absolute WTD error averaged across the 12 test segments. The dashed vertical line marks the approximate lead time at which the relative error ranking changes. Panel (b) shows the corresponding comparison for Segment 9.

6.4 Zero-Shot Cross-Basin Performance

The overall mean errors, E, were 0.106 m in Hejiang and 0.099 m in the UBRB. At a lead time of 720 h, the across-segment mean errors, $E_{t=720}$, were 0.154 m in Hejiang and 0.152 m in the UBRB (**Figure 7a**). These results show that the model maintained an aggregate long-horizon error level

comparable to that in the source basin without target-basin training, fine-tuning, or recalculation of the standardization statistics. Performance nevertheless varied among individual segments. Three representative cases are shown in **Figure 7b–d**, and results for all 12 segments are provided in **Figure S5**. In Segment 2, where precipitation was relatively low in both basins, the segment-mean error, E_i, in Hejiang was 27.2% higher than that in the UBRB. The corresponding E_i values differed by less than 1% in Segment 5. In the precipitation-active Segment 9, by contrast, the E_i and final-hour error in Hejiang were 9.2% and 30.9% lower than those in the UBRB, respectively.

The UBRB and Hejiang are geographically adjacent and have broadly similar hydroclimatic and hydrogeological settings, making this a favorable but meaningful test of regional cross-basin transfer. The comparable errors provide initial and encouraging evidence that the adapted PredFormer can be applied beyond its training basin without fine-tuning, but they do not yet establish general transferability. Although constructing and running the additional high-resolution ParFlow-CLM simulations required for such tests is resource intensive, future work should extend the evaluation to basins with more contrasting hydroclimatic and hydrogeological conditions.

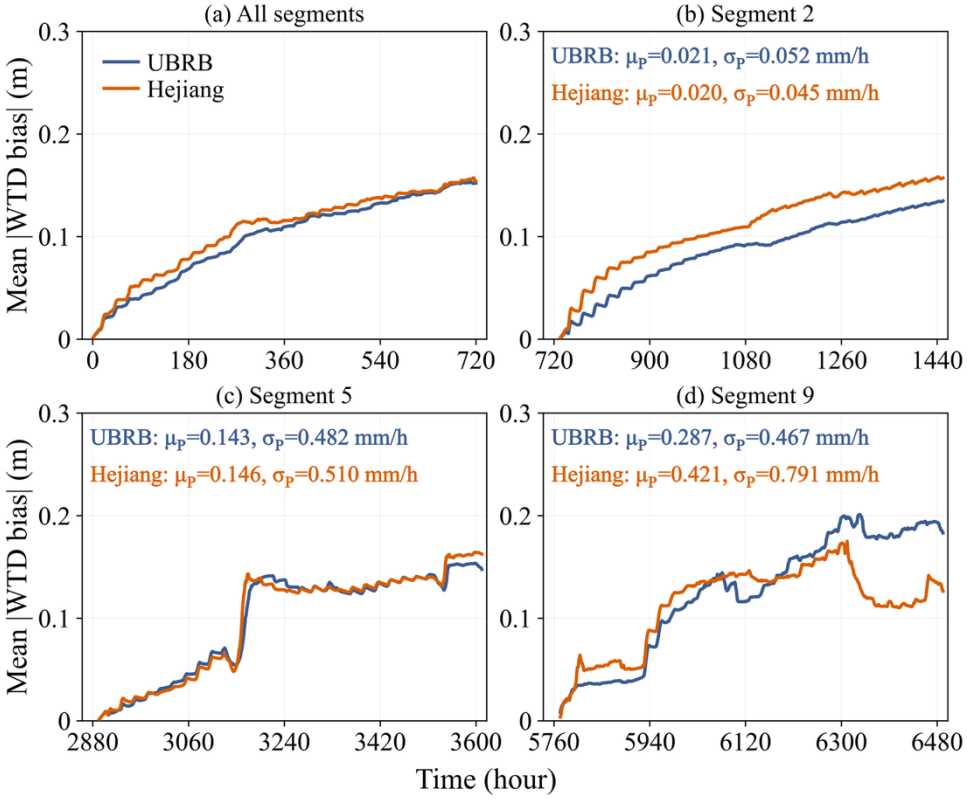


Figure 7. Zero-shot cross-basin performance of the UBRB-trained PredFormer in Hejiang during WY2021. Panel (a) compares the spatial-mean absolute WTD error averaged across the 12 test segments as a function of lead time, and panels (b–d) show the corresponding error trajectories for Segments 2, 5, and 9, respectively. Blue and orange curves represent the UBRB and Hejiang, respectively, and annotations report the mean (μ_P) and standard deviation (σ_P) of domain-mean hourly precipitation within each segment. The model was trained using only the unperturbed UBRB WY2019–WY2020 simulations and applied to Hejiang without target-basin training, fine-tuning, or recalculation of the standardization statistics.

6.5 Effects of Precipitation-Regime Data Augmentation

The reference simulations showed that stronger precipitation regimes were associated with larger and more variable hourly changes in domain-mean WTD, defined as $\Delta\mathrm{WTD}_t = \mathrm{WTD}_t - \mathrm{WTD}_{t-1}$, with each hourly change assigned to the precipitation regime of its corresponding 24 h window (**Figure S6**). As the precipitation regime increased from Dry to Heavy, the distribution of ΔWTD shifted toward more negative values and became wider. Because WTD is defined as depth below the land surface, negative ΔWTD indicates a rising water table. The greater variability under stronger precipitation regimes suggests a more demanding prediction problem and motivated the precipitation-regime-specific data-augmentation experiments. The augmentation strategies produced different long-horizon error trajectories across the 12 segments (**Figure S7**). Averaged over all lead times and segments (**Figure 8a**), All-1.4× produced the lowest overall mean error, *E*, decreasing it slightly from 0.111 m for the baseline to 0.108 m. Heavy-all produced a comparable overall error, whereas Dry-1000 and ModHeavy-1000 performed less well in the overall comparison. These relatively small differences in the overall averages, however, concealed much stronger regime-dependent responses.

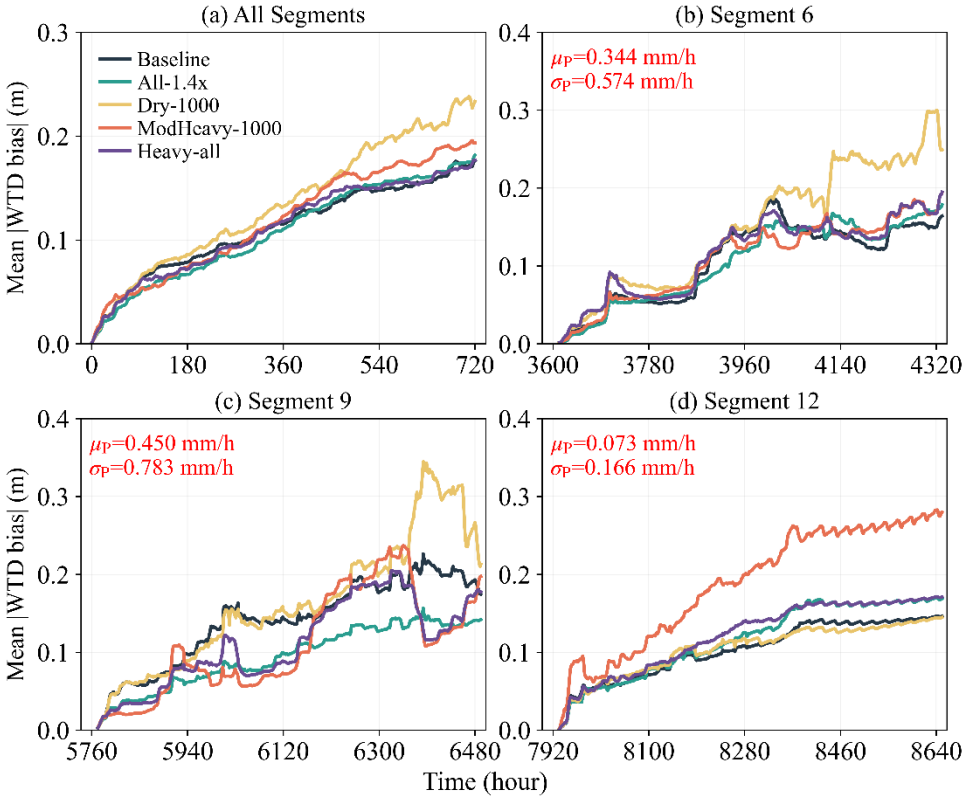


Figure 8. Effects of precipitation-regime data augmentation on 720 h autoregressive WTD prediction in the independent WY2019 test simulation. Panel (a) shows the spatial-mean absolute WTD error averaged across the 12 test segments, and panels (b–d) show the same metric for Segments 6, 9, and 12, respectively. The baseline model was trained using the unperturbed WY2020–WY2021 ParFlow-CLM simulations, whereas the augmented models additionally used samples generated from precipitation-perturbed WY2020–WY2021 simulations. Red annotations in panels (b–d) report the mean (μ_P) and standard deviation (σ_P) of domain-mean hourly precipitation within the respective segments.

At the segment level, augmentation was most beneficial when the added training samples were relevant to the precipitation conditions encountered during prediction. In Segment 6 (**Figure 8b**), which experienced intermediate precipitation activity, All-1.4× performed similarly to the baseline, whereas Dry-1000 increased the error. In the precipitation-active Segment 9 (**Figure 8c**), All-1.4× reduced the mean error, E_i, from 0.141 to 0.095 m, and the ModHeavy-1000 and Heavy-all strategies also outperformed the baseline. By contrast, Dry-1000 produced the largest error in this segment. Segment 12 (**Figure 8d**) exhibited the opposite behavior under relatively weak precipitation forcing: the baseline and Dry-1000 performed similarly, whereas the strategies emphasizing stronger precipitation regimes increased the error. Thus, no single augmentation strategy consistently improved prediction across all segments.

To examine this regime dependence more directly, the hourly error increments, $\Delta E_{i,t}$, from all 12 segments were pooled and stratified according to the precipitation regime of the corresponding 24 h windows (**Figure 9**). Under Heavy-regime windows, ModHeavy-1000 and Heavy-all shifted the mean $\Delta E_{i,t}$ from positive baseline values to negative values, indicating that the error decreased, on average, relative to the preceding hour. For Dry-regime windows, Dry-1000 also reduced the mean $\Delta E_{i,t}$ relative to the baseline, although its overall mean error, E, remained higher than that of the baseline (**Figure 8a**). Regime-specific augmentation may therefore improve error propagation without necessarily producing a lower error over the complete rollout.

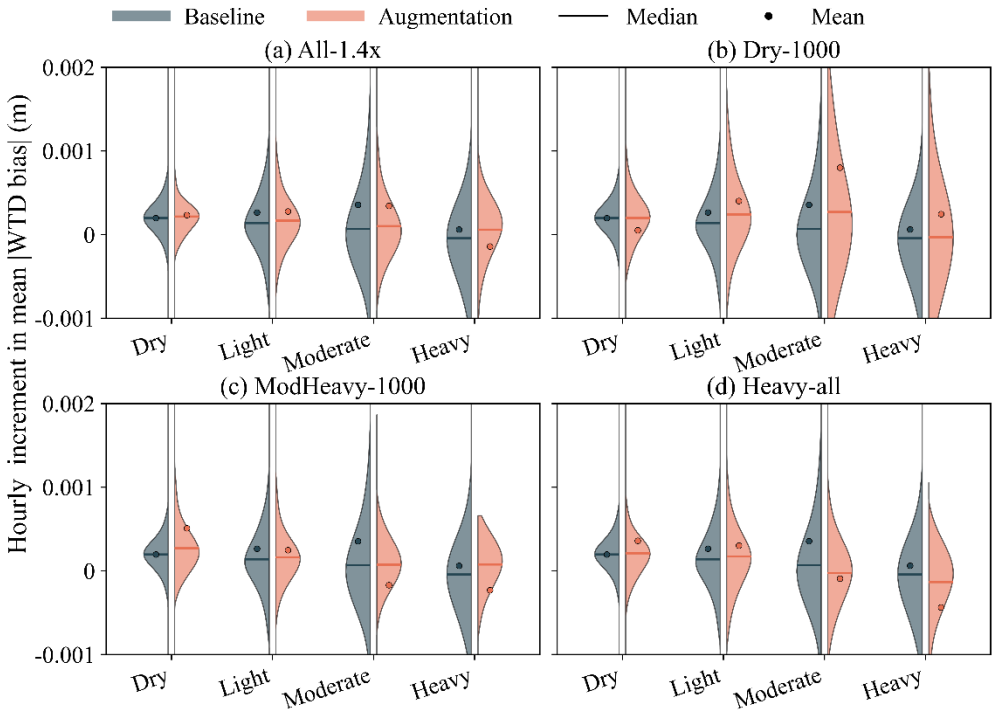


Figure 9. Effects of precipitation-regime data augmentation on hourly changes in WTD prediction error. Panels (a–d) compare the baseline model with models trained using the All-1.4×, Dry-1000, ModHeavy-1000, and Heavy-all augmentation strategies, respectively. Within each panel, the distributions are stratified into Dry, Light, Moderate, and Heavy precipitation regimes. The distributions were calculated from the 12 test segments of the unperturbed WY2019 simulation. Precipitation regimes were assigned using consecutive, non-overlapping 24 h windows classified according to domain-mean accumulated precipitation (P_{24}). The hourly error increment was defined as $\Delta E_{i,t} = E_{i,t} - E_{i,t-1}$, where

$E_{i,t}$ denotes the spatial-mean absolute WTD error for segment *i* at prediction hour *t*. Positive and negative values indicate increases and decreases in error relative to the preceding hour, respectively. Gray and orange violins represent the baseline and augmented models, respectively, while horizontal lines and points indicate the median and mean.

Together, these results demonstrate that process-consistent data augmentation is potentially useful, but its benefit depends on the correspondence between the precipitation regimes represented in the augmented training data and those encountered during prediction. More broadly, the results indicate that augmentation should target underrepresented hydrometeorological conditions rather than simply increase the total number of training samples (Xie et al., 2021). Models trained to emphasize Dry, Moderate, or Heavy precipitation conditions could be selected or combined according to the anticipated forcing regime. For operational groundwater prediction and water-resources management, this regime dependence also suggests a possible multi-model or regime-adaptive framework rather than reliance on a single universally augmented model.

7. Conclusions

This study developed and systematically evaluated a Transformer-based surrogate for distributed regional groundwater dynamics by adapting PredFormer to multilayer pressure-head prediction using ParFlow-CLM simulations. The framework reformulated PredFormer for pressure-residual prediction, incorporated prescribed PME forcing and static hydrogeological attributes, and introduced overlapping spatial windowing to reconstruct predictions over complete regional domains. Model development and systematic evaluation, including precipitation-regime-specific data augmentation, were conducted over the approximately 34,000 km² UBRB, and zero-shot cross-basin transfer was further evaluated over a Hejiang simulation domain spanning approximately 24,000 km². The resulting model generated continuous 720 h predictions of distributed multilayer pressure-head fields without introducing ParFlow-CLM reference states for correction after initialization.

Across the 720 h UBRB test segments, prediction errors generally increased with lead time but exhibited distinct temporal and spatial patterns. Larger upper-tail spatial errors were more closely associated with segment-scale precipitation amount and variability, whereas pronounced fluctuations in the error trajectories frequently coincided with abrupt wet–dry transitions. PredRNN was more accurate during the early prediction period, but PredFormer produced lower errors and smoother error trajectories over longer autoregressive horizons, indicating that the benefit of the Transformer architecture emerged primarily at extended lead times. In the zero-shot evaluation, the UBRB-trained model was applied directly to Hejiang without target-basin training, fine-tuning, or recalculation of the standardization statistics. The overall mean error was 0.106 m in Hejiang, close to the 0.099 m obtained in the UBRB, while the corresponding across-segment mean errors at 720 h were 0.154 and 0.152 m. These results provide initial evidence that the adapted PredFormer can retain comparable long-horizon performance when transferred to a neighboring regional basin.

The contribution of additional inputs depended strongly on groundwater depth. Prescribed PME was the most influential additional input overall, reducing the mean absolute WTD error from 0.151 to 0.099 m relative to pressure head alone. Its contribution was greatest in shallow-WTD areas, whereas

static hydrogeological attributes were most beneficial in the intermediate WTD zone. For WTD greater than 20 m, pressure head alone produced the lowest error, indicating that deep-groundwater predictions depended primarily on the antecedent state, with limited additional benefit from short-term surface forcing or explicit static attributes over the evaluated horizon. The method used to integrate static information had a smaller but systematic influence. Post-temporal–spatial cross-attention achieved the lowest overall error and reduced the final 720 h error by 10.2% relative to direct raw-static concatenation. This result supports a fusion sequence in which temporal evolution and spatial interactions are first encoded and the resulting dynamic representation is subsequently conditioned on static attributes.

Process-consistent data augmentation produced relatively small changes in overall average error but clear precipitation-regime-dependent effects. Adding Moderate–Heavy or Heavy samples reduced hourly error accumulation under Heavy-precipitation conditions, whereas Dry augmentation reduced error accumulation during Dry conditions without consistently lowering the absolute WTD error over the complete prediction horizon. These findings indicate that augmentation should be designed to improve the representation of underrepresented hydrometeorological conditions rather than simply increase the total number of training samples. They also suggest the potential value of regime-adaptive or multi-model prediction frameworks in which models trained for different hydrometeorological conditions are selected or combined according to anticipated forcing regimes.

The present study focused on model development and detailed process evaluation in one regional source basin using a three-year simulation record and a 720 h prediction horizon. The additional zero-shot evaluation in Hejiang showed that comparable long-horizon performance could be retained in a neighboring basin with broadly similar hydroclimatic and hydrogeological settings. Building on this result, future work should extend the zero-shot evaluation to basins with more contrasting hydroclimatic and hydrogeological conditions, although doing so will require constructing additional high-resolution ParFlow-CLM domains and conducting the corresponding resource-intensive simulations. Additional directions include examining longer training records and prediction horizons and investigating whether groundwater data assimilation can improve state initialization and constrain long-horizon prediction errors. Extending the present offline framework toward the use of forecast forcing or interactive coupling with land-surface models would further clarify its operational applicability. Overall, this study provides a systematic basis for understanding when Transformer-based groundwater surrogates are most effective and how long-horizon error evolution, input composition, static-information fusion, cross-basin transfer, groundwater depth, and training-sample coverage influence their performance. These findings provide practical guidance for developing computationally efficient tools for regional groundwater prediction and water-resources management.

Conflict of Interest

The authors declare no conflicts of interest relevant to this study.

Open Research

The source code for training and inference of the PredFormer-based groundwater surrogate is publicly available at https://github.com/HH12138666/ParFlow-transformer, and the version used in this

794 study is archived at https://doi.org/10.5281/zenodo.23587543. The unperturbed ParFlow-CLM
795 simulations used to construct the baseline dataset are available at
796 https://doi.org/10.57760/sciencedb.46348. The precipitation-perturbed simulations, Hejiang reference
797 simulations and model predictions, trained checkpoints, normalization statistics, and scripts and source
798 data for analysis and figure generation are available in a supporting dataset at
799 https://doi.org/10.57760/sciencedb.0106u.

References

Asher, M. J., Croke, B. F. W., Jakeman, A. J., & Peeters, L. J. M. (2015). A review of surrogate models and their application to groundwater modeling. *Water Resources Research, 51*(8), 5957–5973. https://doi.org/10.1002/2015WR016967

Bauer, P., Thorpe, A., & Brunet, G. (2015). The quiet revolution of numerical weather prediction. *Nature, 525*(7567), 47–55. https://www.nature.com/articles/nature14956

Bennett, A., Tran, H., De la Fuente, L., Triplett, A., Ma, Y., Melchior, P., et al. (2024). Spatio-Temporal Machine Learning for Regional to Continental Scale Terrestrial Hydrology. *Journal of Advances in Modeling Earth Systems, 16*(6), e2023MS004095. https://agupubs.onlinelibrary.wiley.com/doi/10.1029/2023MS004095

Bi, K., Xie, L., Zhang, H., Chen, X., Gu, X., & Tian, Q. (2023). Accurate medium-range global weather forecasting with 3D neural networks. *Nature, 619*(7970), 533–538. https://www.nature.com/articles/s41586-023-06185-3

Bodnar, C., Bruinsma, W. P., Lucic, A., Stanley, M., Allen, A., Brandstetter, J., et al. (2025). A foundation model for the Earth system. *Nature, 641*(8065), 1180–1187. https://www.nature.com/articles/s41586-025-09005-y

Chen, Y., Liu, G., Huang, X., Chen, K., Hou, J., & Zhou, J. (2021). Development of a surrogate method of groundwater modeling using gated recurrent unit to improve the efficiency of parameter auto-calibration and global sensitivity analysis. *Journal of Hydrology, 598*, 125726. https://www.sciencedirect.com/science/article/pii/S0022169420311872

Condon, L. E., Kollet, S., Bierkens, M. F. P., Fogg, G. E., Maxwell, R. M., Hill, M. C., et al. (2021). Global Groundwater Modeling and Monitoring: Opportunities and Challenges. *Water Resources Research, 57*(12), e2020WR029500. https://agupubs.onlinelibrary.wiley.com/doi/10.1029/2020WR029500

Cuthbert, M. O., Gleeson, T., Moosdorf, N., Befus, K. M., Schneider, A., Hartmann, J., & Lehner, B. (2019). Global patterns and dynamics of climate–groundwater interactions. *Nature Climate Change, 9*(2), 137–141. https://doi.org/10.1038/s41558-018-0386-4

Dai, T., Maher, K., & Perzan, Z. (2025). Machine learning surrogates for efficient hydrologic modeling: Insights from stochastic simulations of managed aquifer recharge. *Journal of Hydrology, 652*, 132606. https://www.sciencedirect.com/science/article/pii/S002216942402002X

Devlin, J., Chang, M.-W., Lee, K., & Toutanova, K. (2019). *BERT: Pre-training of Deep Bidirectional Transformers for Language Understanding.* Paper presented at the Proceedings of the 2019 Conference of the North American Chapter of the Association for Computational Linguistics: Human Language Technologies, Volume 1 (Long and Short Papers).

do Lago, C. A. F., Giacomoni, M. H., Bentivoglio, R., Taormina, R., Gomes, M. N. J., & Mendiondo, E. M. (2023). Generalizing rapid flood predictions to unseen urban catchments with conditional generative adversarial networks. *Journal of Hydrology, 618*, 129276. https://doi.org/10.1016/j.jhydrol.2023.129276

Dosovitskiy, A., Beyer, L., Kolesnikov, A., Weissenborn, D., Zhai, X., Unterthiner, T., et al. (2021). *An Image is Worth 16x16 Words: Transformers for Image Recognition at Scale.* Paper presented at the International Conference on Learning Representations.

Gao, Z., Shi, X., Wang, H., Zhu, Y., Wang, Y., Li, M., & Yeung, D.-Y. (2022). *Earthformer: Exploring Space-Time Transformers for Earth System Forecasting.* Paper presented at the Advances in neural

information processing systems.

Heidari, E., & Khan, A. A. (2026). Probabilistic Sub-Daily Streamflow Forecasting in Data-Scarce Catchments Through a Zero-Shot Inductive Transfer Learning Approach. *JAWRA Journal of the American Water Resources Association, 62*(2), e70115. https://onlinelibrary.wiley.com/doi/10.1111/1752-1688.70115

Hersbach, H., Bell, B., Berrisford, P., Hirahara, S., Horányi, A., Muñoz-Sabater, J., et al. (2020). The ERA5 global reanalysis. *Quarterly Journal of the Royal Meteorological Society, 146*(730), 1999–2049. https://rmets.onlinelibrary.wiley.com/doi/10.1002/qj.3803

Heudorfer, B., Liesch, T., & Broda, S. (2024). On the challenges of global entity-aware deep learning models for groundwater level prediction. *Hydrology and Earth System Sciences, 28*(3), 525–543. https://hess.copernicus.org/articles/28/525/2024/

Hochreiter, S., & Schmidhuber, J. (1997). Long Short-Term Memory. *Neural Computation, 9*(8), 1735–1780. https://doi.org/10.1162/neco.1997.9.8.1735

Jesse, G., Boateng, C. D., Aryee, J. N. A., Osei, M. A., Wemegah, D. D., Gidigasu, S. S. R., et al. (2025). A systematic review of machine learning models for groundwater level prediction. *Applied Computing and Geosciences, 28*, 100303. https://www.sciencedirect.com/science/article/pii/S2590197425000850

Kochkov, D., Yuval, J., Langmore, I., Norgaard, P., Smith, J., Mooers, G., et al. (2024). Neural general circulation models for weather and climate. *Nature, 632*(8027), 1060–1066. https://www.nature.com/articles/s41586-024-07744-y

Kollet, S. J., & Maxwell, R. M. (2006). Integrated surface–groundwater flow modeling: A free-surface overland flow boundary condition in a parallel groundwater flow model. *Advances in Water Resources, 29*(7), 945–958. https://linkinghub.elsevier.com/retrieve/pii/S0309170805002101

Kollet, S. J., & Maxwell, R. M. (2008). Capturing the influence of groundwater dynamics on land surface processes using an integrated, distributed watershed model. *Water Resources Research, 44*(2), W02402. https://agupubs.onlinelibrary.wiley.com/doi/10.1029/2007WR006004

Kratzert, F., Klotz, D., Herrnegger, M., Sampson, A. K., Hochreiter, S., & Nearing, G. S. (2019). Toward Improved Predictions in Ungauged Basins: Exploiting the Power of Machine Learning. *Water Resources Research, 55*(12), 11344–11354. https://agupubs.onlinelibrary.wiley.com/doi/10.1029/2019WR026065

Kuffour, B. N. O., Engdahl, N. B., Woodward, C. S., Condon, L. E., Kollet, S., & Maxwell, R. M. (2020). Simulating coupled surface–subsurface flows with ParFlow v3.5.0: capabilities, applications, and ongoing development of an open-source, massively parallel, integrated hydrologic model. *Geoscientific Model Development, 13*(3), 1373–1397. https://gmd.copernicus.org/articles/13/1373/2020/

Leonarduzzi, E., Tran, H., Bansal, V., Hull, R. B., De la Fuente, L., Bearup, L. A., et al. (2022). Training machine learning with physics-based simulations to predict 2D soil moisture fields in a changing climate. *Frontiers in Water, 4*, 927113. https://www.frontiersin.org/journals/water/articles/10.3389/frwa.2022.927113/full

Li, X., Khandelwal, A., Jia, X., Cutler, K., Ghosh, R., Renganathan, A., et al. (2022). Regionalization in a Global Hydrologic Deep Learning Model: From Physical Descriptors to Random Vectors. *Water Resources Research, 58*(8), e2021WR031794. https://agupubs.onlinelibrary.wiley.com/doi/10.1029/2021WR031794

Liesch, T., & Ohmer, M. (2026). Strategies for incorporating static features into global deep learning

models. *Hydrology and Earth System Sciences, 30*(7), 1877–1890. https://hess.copernicus.org/articles/30/1877/2026/

Liu, J., Shen, C., O'Donncha, F., Song, Y., Zhi, W., Beck, H. E., et al. (2025). From RNNs to Transformers: benchmarking deep learning architectures for hydrologic prediction. *Hydrology and Earth System Sciences, 29*(23), 6811–6828. https://hess.copernicus.org/articles/29/6811/2025/

Loshchilov, I., & Hutter, F. (2017). *SGDR: Stochastic Gradient Descent with Warm Restarts.* Paper presented at the International Conference on Learning Representations.

Loshchilov, I., & Hutter, F. (2019). *Decoupled Weight Decay Regularization.* Paper presented at the International Conference on Learning Representations.

Maxwell, R. M., & Condon, L. E. (2016). Connections between groundwater flow and transpiration partitioning. *Science, 353*(6297), 377–380. https://www.science.org/doi/10.1126/science.aaf7891

Maxwell, R. M., Condon, L. E., & Kollet, S. J. (2015). A high-resolution simulation of groundwater and surface water over most of the continental US with the integrated hydrologic model ParFlow v3. *Geoscientific Model Development, 8*(3), 923–937. https://gmd.copernicus.org/articles/8/923/2015/

Maxwell, R. M., Condon, L. E., & Melchior, P. (2021). A Physics-Informed, Machine Learning Emulator of a 2D Surface Water Model: What Temporal Networks and Simulation-Based Inference Can Help Us Learn about Hydrologic Processes. *Water, 13*(24), 3633. https://www.mdpi.com/2073-4441/13/24/3633

Maxwell, R. M., & Kollet, S. J. (2008). Interdependence of groundwater dynamics and land-energy feedbacks under climate change. *Nature Geoscience, 1*(10), 665–669. https://www.nature.com/articles/ngeo315

Maxwell, R. M., & Miller, N. L. (2005). Development of a Coupled Land Surface and Groundwater Model. *Journal of Hydrometeorology, 6*(3), 233–247. https://journals.ametsoc.org/doi/10.1175/JHM422.1

Muñoz-Sabater, J., Dutra, E., Agustí-Panareda, A., Albergel, C., Arduini, G., Balsamo, G., et al. (2021). ERA5-Land: a state-of-the-art global reanalysis dataset for land applications. *Earth System Science Data, 13*(9), 4349–4383. https://essd.copernicus.org/articles/13/4349/2021/

Nguyen, T., Brandstetter, J., Kapoor, A., Gupta, J. K., & Grover, A. (2023). *ClimaX: A foundation model for weather and climate.* Paper presented at the Proceedings of the 40th International Conference on Machine Learning.

Ohmer, M., & Liesch, T. (2026). Never Train a Deep Learning Model on a Single Well? Revisiting Training Strategies for Groundwater Level Prediction. *Hydrology and Earth System Sciences, 30*(8), 2373–2394. https://hess.copernicus.org/articles/30/2373/2026/

Rasiya Koya, S., & Roy, T. (2024). Temporal Fusion Transformers for streamflow Prediction: Value of combining attention with recurrence. *Journal of Hydrology, 637*, 131301. https://www.sciencedirect.com/science/article/pii/S0022169424006966

Rasp, S., Dueben, P. D., Scher, S., Weyn, J. A., Mouatadid, S., & Thuerey, N. (2020). WeatherBench: A Benchmark Data Set for Data-Driven Weather Forecasting. *Journal of Advances in Modeling Earth Systems, 12*(11), e2020MS002203. https://agupubs.onlinelibrary.wiley.com/doi/10.1029/2020MS002203

Reichstein, M., Camps-Valls, G., Stevens, B., Jung, M., Denzler, J., Carvalhais, N., & Prabhat. (2019). Deep learning and process understanding for data-driven Earth system science. *Nature, 566*(7743), 195–204. https://www.nature.com/articles/s41586-019-0912-1

Shazeer, N. (2020). *GLU Variants Improve Transformer*. arXiv. Retrieved from

https://arxiv.org/abs/2002.05202

Shi, X., Chen, Z., Wang, H., Yeung, D.-Y., Wong, W.-k., & Woo, W.-c. (2015). *Convolutional LSTM Network: A Machine Learning Approach for Precipitation Nowcasting.* Paper presented at the Advances in neural information processing systems.

Smith, L. N., & Topin, N. (2019). *Super-convergence: very fast training of neural networks using large learning rates.* Paper presented at the Artificial Intelligence and Machine Learning for Multi-Domain Operations Applications.

Sun, A., Tang, Z., Zheng, C., Shangguan, W., & Yang, C. (2026). What Can We Learn from a Reduced-Dimensional Groundwater Representation for Diagnosing Groundwater–Land Interactions? Insights from the Water Table Ratio. *EarthArXiv*. https://eartharxiv.org/repository/view/14463/

Sun, X., Zhong, X., Xu, X., Huang, Y., Li, H., Neelin, J. D., et al. (2025). A data-to-forecast machine learning system for global weather. *Nature Communications, 16*(1), 6658. https://www.nature.com/articles/s41467-025-62024-1

Tang, Y., Qi, L., Li, X., Ma, C., & Yang, M.-H. (2026). Video Prediction Transformers without Recurrence or Convolution. *Transactions on Machine Learning Research*. https://openreview.net/forum?id=Afvhu9Id8m

Tran, H., Leonarduzzi, E., De la Fuente, L., Hull, R. B., Bansal, V., Chennault, C., et al. (2021). Development of a Deep Learning Emulator for a Distributed Groundwater–Surface Water Model: ParFlow-ML. *Water, 13*(23), 3393. https://www.mdpi.com/2073-4441/13/23/3393

van Genuchten, M. T. (1980). A Closed-form Equation for Predicting the Hydraulic Conductivity of Unsaturated Soils. *Soil science society of America journal, 44*(5), 892–898. https://acsess.onlinelibrary.wiley.com/doi/10.2136/sssaj1980.03615995004400050002x

Vaswani, A., Shazeer, N., Parmar, N., Uszkoreit, J., Jones, L., Gomez, A. N., et al. (2017). *Attention Is All You Need.* Paper presented at the Advances in neural information processing systems.

Wang, Y., Long, M., Wang, J., Gao, Z., & Yu, P. S. (2017). *PredRNN: Recurrent Neural Networks for Predictive Learning using Spatiotemporal LSTMs.* Paper presented at the Advances in neural information processing systems.

Wang, Y., Wu, H., Zhang, J., Gao, Z., Wang, J., Yu, P. S., & Long, M. (2023). PredRNN: A Recurrent Neural Network for Spatiotemporal Predictive Learning. *IEEE Transactions on Pattern Analysis and Machine Intelligence, 45*(2), 2208–2225. https://ieeexplore.ieee.org/document/9749915/

Xie, K., Liu, P., Zhang, J., Han, D., Wang, G., & Shen, C. (2021). Physics-guided deep learning for rainfall-runoff modeling by considering extreme events and monotonic relationships. *Journal of Hydrology, 603*, 127043. https://www.sciencedirect.com/science/article/pii/S0022169421010933

Xu, W., Chen, J., & Corzo, G. (2025). Combining data augmentation and hybrid modeling approaches for deep learning-based monthly streamflow forecasting. *Journal of Hydrology, 659*, 133318. https://linkinghub.elsevier.com/retrieve/pii/S0022169425006560

Yang, C., Huang, H., Tang, Z., Dai, Y., & Chang, X. (2026). A hybrid physics–ML framework for integrating groundwater dynamics into land surface modeling. *EGUsphere, 2026*, 1.

Yang, C., Jia, Z., Xu, W., Wei, Z., Zhang, X., Zou, Y., et al. (2025). CONCN: a high-resolution, integrated surface water–groundwater ParFlow modeling platform of continental China. *Hydrology and Earth System Sciences, 29*(9), 2201–2218. https://hess.copernicus.org/articles/29/2201/2025/

Yang, C., Sun, A., Zhang, S., Dai, Y., Kollet, S., & Maxwell, R. (2026). 20 years of trials and insights: bridging legacy and next generation in ParFlow and Land Surface Model Coupling. *Geoscientific*

Model Development, 19(5), 1849–1866. https://gmd.copernicus.org/articles/19/1849/2026/

Supporting Information

Text S1. Detailed Formulation and Implementation of the Groundwater-Adapted PredFormer

This section presents the architectural formulations underlying the groundwater-adapted PredFormer. Sections S1.1–S1.3 describe patch tokenization and positional encoding, gated Transformer blocks (GTBs), and temporal-first factorized attention, respectively. Groundwater-specific static fusion, residual prediction, blockwise autoregressive rollout, loss calculation, spatial reconstruction, and training settings are described in the main text.

S1.1 Patch Tokenization and Positional Encoding

To reduce GPU memory usage, the gridded pressure-head and prescribed PME fields were processed in local spatial windows rather than as a single domain-wide Transformer input. Adjacent windows overlapped to retain spatial context across partition boundaries and reduce boundary artifacts in the reconstructed fields. Each window was divided into non-overlapping $p \times p$ patches, where p is the number of grid cells along each side of a patch. At input time step t, the n-th patch was flattened and linearly projected as

$$z_{t,n} = W_e \mathrm{vec}(x_{t,n}) + b_e + e_{t,n}.$$

Here, $x_{t,n}$ denotes the multichannel input patch at time step t and spatial position n, $z_{t,n}$ is its D-dimensional token embedding, vec denotes vectorization, W_e is the learnable embedding matrix, b_e is the learnable bias vector, and $e_{t,n}$ encodes the temporal and spatial position of the patch. The resulting token tensor for each local window is

$$Z \in \mathbb{R}^{B \times T \times N \times D},$$

where B is the batch size, T is the number of input time steps, N is the number of spatial patches per time step, and D is the token dimension. Spatial windows contained 80 × 64 grid cells along the x and y directions, respectively, with corresponding strides of 40 and 32 cells. Additional boundary-aligned windows were included where necessary to ensure complete domain coverage. Each window was divided into 8 × 8 patches, yielding a 10 × 8 grid of patches and 80 spatial tokens per time step.

S1.2 Gated Transformer Blocks

Within each GTB, multi-head self-attention is used to extract dependencies among tokens. A single attention head is defined as:

$$\mathrm{Attention}(Q, K, V) = \mathrm{Softmax}\left(\frac{QK^T}{\sqrt{d_k}}\right)V,$$

where Q, K, and V are the query, key, and value projections of the input tokens, respectively, and d_k is

the dimension of the key vectors in each attention head. The square root of d_k scales the attention scores. The outputs from multiple attention heads are concatenated and linearly mapped to form multi-head self-attention. The feed-forward component uses the SwiGLU gating structure adopted in PredFormer:

$$\mathrm{SwiGLU}(x) = W_2\left[\mathrm{SiLU}(W_g x + b_g) \odot (W_z x + b_z)\right] + b_2,$$

where $x \in \mathbb{R}^D$ denotes an input token, $\odot$ denotes element-wise multiplication, and SiLU denotes the sigmoid linear unit activation function. The matrices W_g, W_z, and W_2 are learnable weights, and b_g, b_z, and b_2 are learnable bias vectors. The l-th GTB is written as

$$Y^l = Z^l + \mathrm{DropPath}\{\mathrm{MSA}[\mathrm{LN}(Z^l)]\},$$

$$Z^{l+1} = Y^l + \mathrm{DropPath}\{\mathrm{SwiGLU}[\mathrm{LN}(Y^l)]\},$$

where MSA denotes multi-head self-attention and LN denotes layer normalization. Z^l, Y^l, and Z^{l+1} denote the input, post-attention representation, and output of the l-th GTB, respectively. Residual connections facilitate gradient propagation, and DropPath regularizes the network during training.

Within the factorized PredFormer encoder, temporal GTBs apply self-attention across the input time steps for each spatial patch, whereas spatial GTBs apply self-attention across the spatial patches at each time step.

S1.3 Temporal-First Factorized Attention

A temporal-first factorized encoder was used to reduce the computational cost of full spatiotemporal attention while retaining separate temporal and spatial feature extraction. The model first applies temporal attention to each spatial patch across the input time steps and then applies spatial attention across patches at each time step:

$$H = T_S[T_T(Z)],$$

where Z is the input token representation, H is the output representation, and T_T and T_S denote the temporal and spatial Transformer encoders, respectively.

For temporal attention, the token tensor is rearranged so that the T tokens associated with each spatial patch form an attention sequence. The temporal encoder learns how the joint representation of pressure head and prescribed PME forcing evolves over the input period for each spatial patch. The resulting tokens are then rearranged so that the N spatial tokens at each time step form an attention sequence for the spatial encoder. Spatial attention captures dependencies across patches in this joint representation.

The temporal and spatial encoders each contain six GTBs. By replacing joint attention over all $T \times N$ spatiotemporal tokens with separate temporal and spatial attention operations, the factorized

design reduces the computational cost of attention for large gridded groundwater fields.

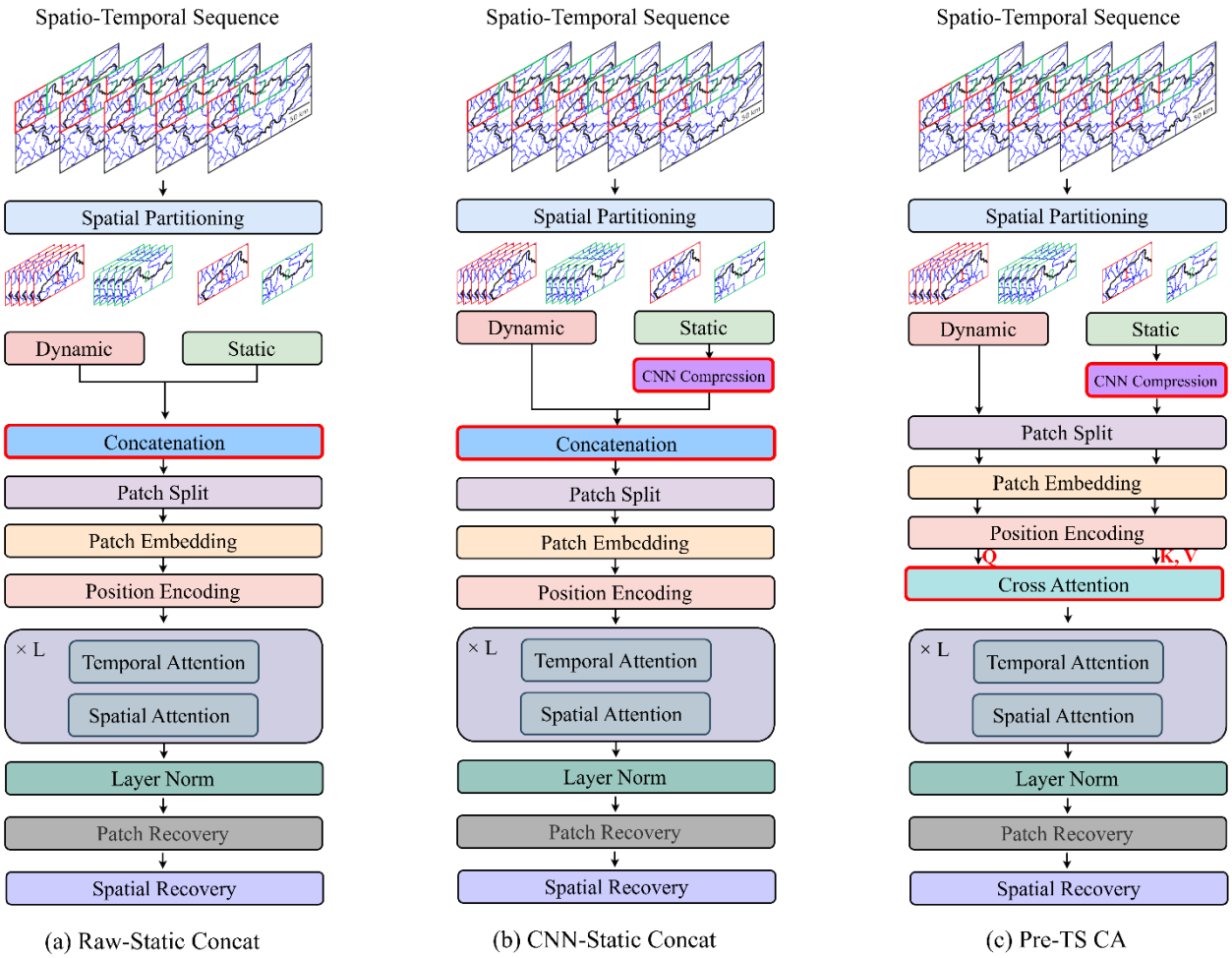


Figure S1. Alternative dynamic-static fusion architectures evaluated for the groundwater-adapted PredFormer. Panels (a–c) show Raw-Static Concatenation, CNN-Compressed Static Concatenation, and Pre-TS Cross-Attention, respectively. In panel (a), the original static attributes are concatenated with the dynamic inputs before patch tokenization. In panel (b), the static attributes are first compressed using a convolutional neural network (CNN) encoder and then concatenated with the dynamic inputs. In panel (c), the dynamic tokens query the CNN-compressed static tokens through cross-attention before temporal-first factorized attention, with dynamic tokens providing queries (Q) and static tokens providing keys (K) and values (V). All configurations share the same PredFormer backbone. Red outlines highlight the modules that differ among the configurations. CA denotes cross-attention, and TS denotes temporal–spatial encoding. The Post-TS Cross-Attention configuration used in the main experiments is shown in Figure 2.

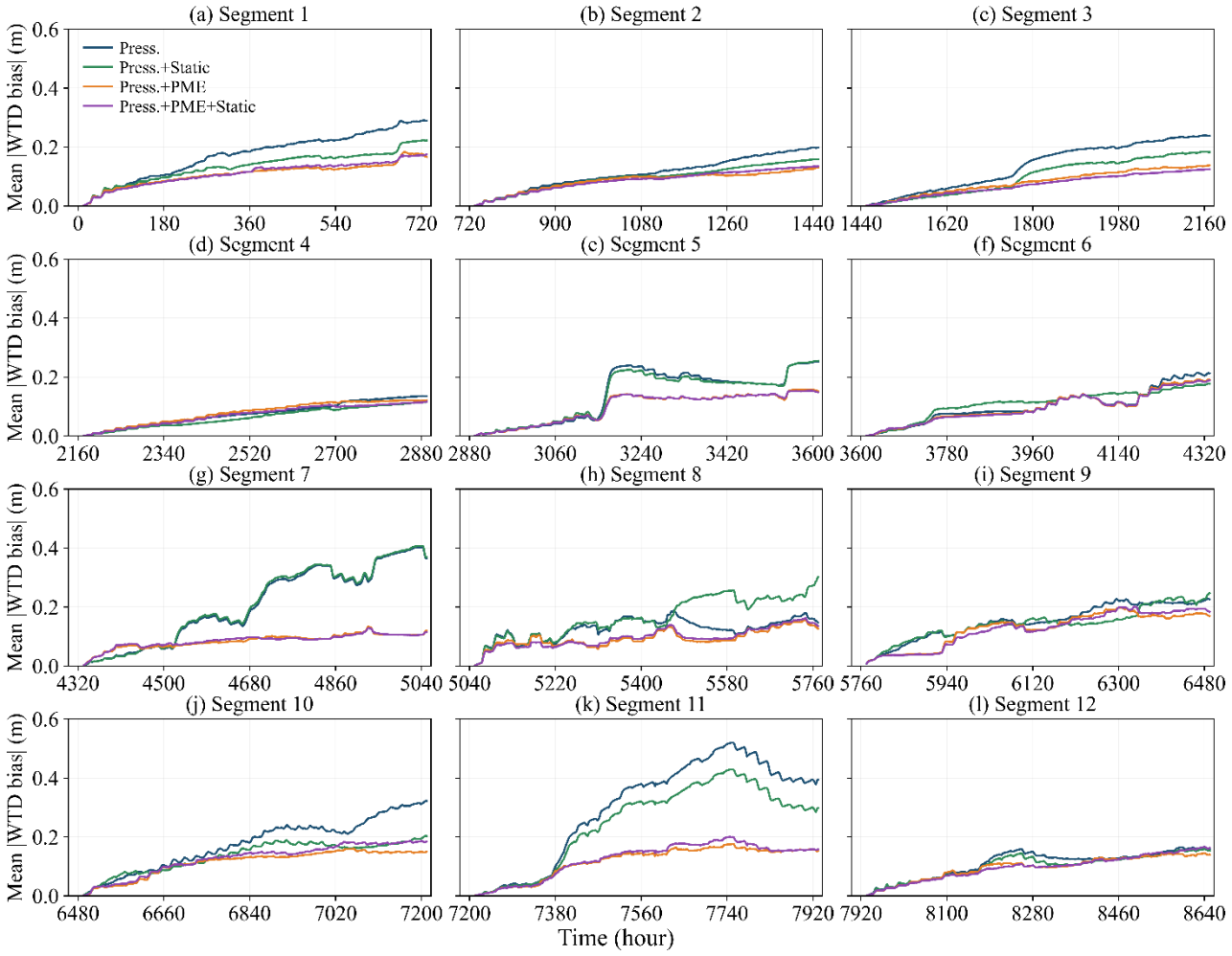


Figure S2. Segment-wise effects of input composition on 720 h autoregressive WTD prediction in the UBRB during WY2021. Panels (a–l) show the 12 independently initialized, non-overlapping 720 h test segments. Curves compare Press., Press. + Static, Press. + PME, and Press. + PME + Static. Press. denotes pressure head, PME denotes prescribed layer-resolved P−ET source–sink forcing, and Static denotes static attributes. Each segment was initialized using the immediately preceding 12 h of ParFlow-CLM reference pressure-head fields. Predicted 12 h pressure-head blocks were then fed back recursively without reintroducing reference pressure-head states. For configurations including PME, the prescribed PME forcing was supplied throughout rollout; static attributes, when included, remained fixed. Each curve shows the spatial mean absolute WTD error at each forecast hour. The horizontal axis shows simulation time in hours.

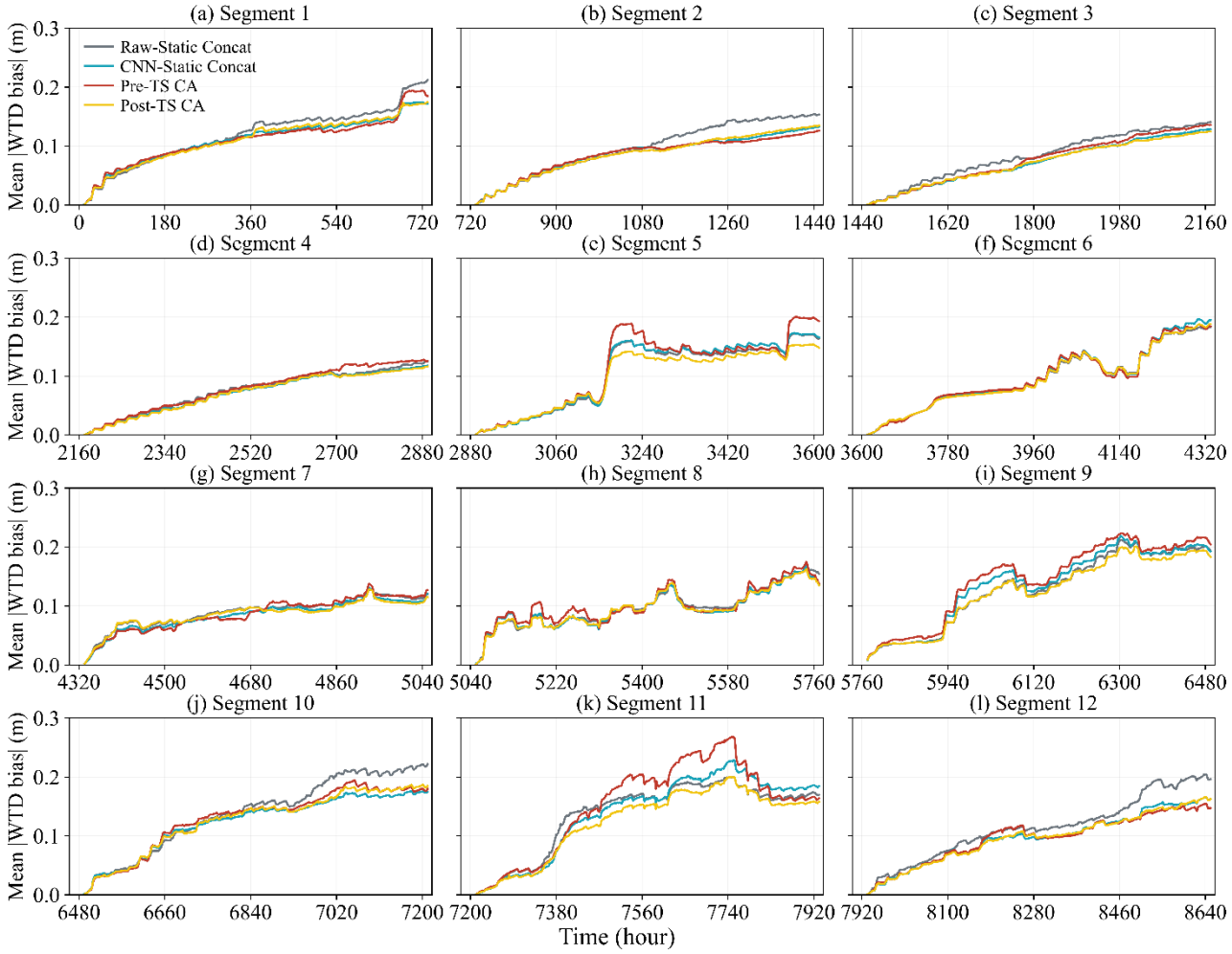


Figure S3. Segment-wise effects of dynamic-static fusion strategies on 720 h autoregressive WTD prediction in the UBRB during WY2021. Panels (a–l) show the 12 independently initialized, non-overlapping 720 h test segments. Curves compare Raw-Static Concatenation, CNN-Compressed Static Concatenation, Pre-TS Cross-Attention, and Post-TS Cross-Attention. All configurations used the complete Press. + PME + Static input combination and the same data split and training procedure. Each segment was initialized using the immediately preceding 12 h of ParFlow-CLM reference pressure-head fields, after which predicted 12 h pressure-head blocks were fed back recursively without reference-state correction. Each curve shows the spatial mean absolute WTD error at each forecast hour. The horizontal axis shows simulation time in hours. CA denotes cross-attention; the fusion configurations are illustrated in Figure 2 and Figure S1.

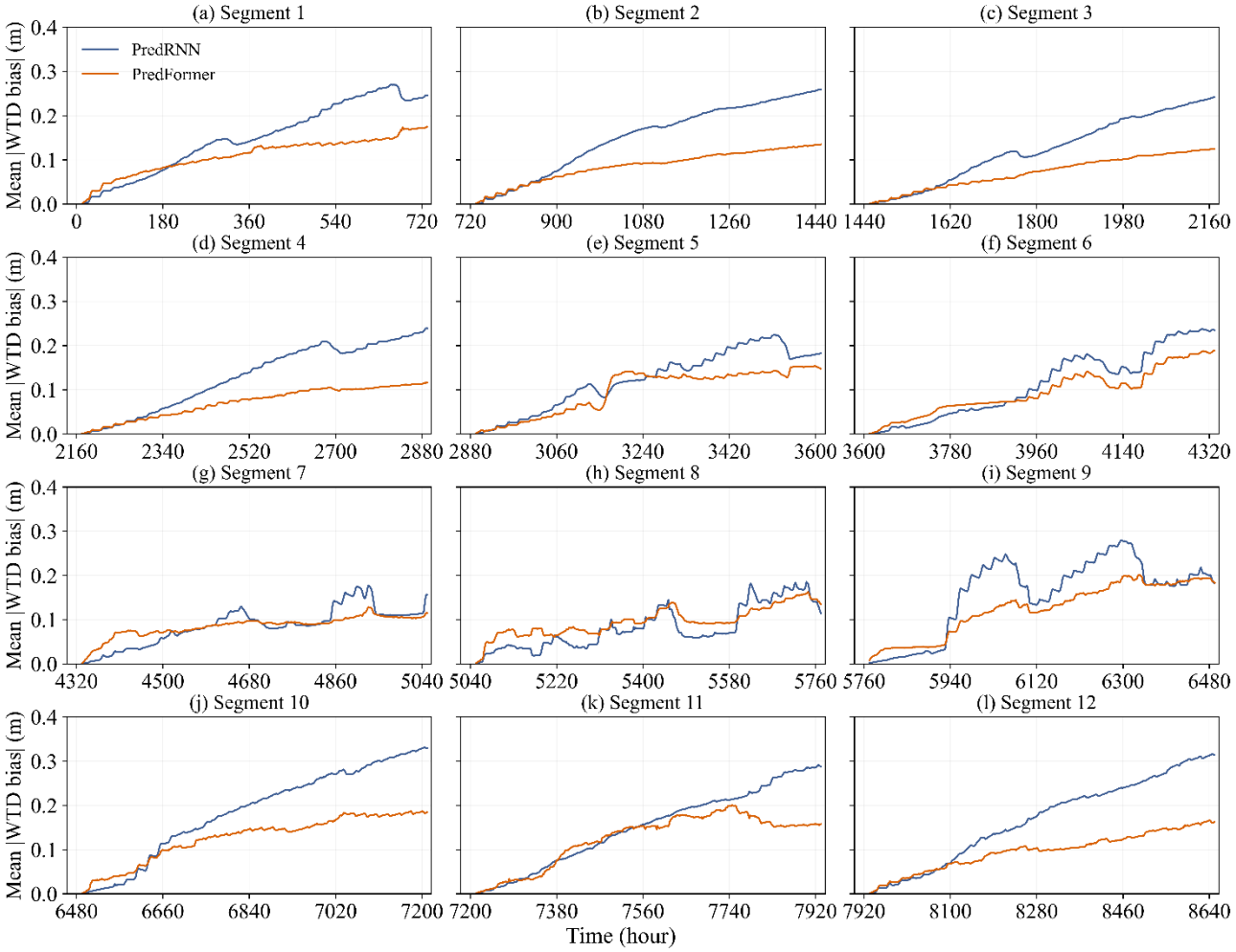


Figure S4. Segment-wise comparison of PredFormer and the PredRNN recurrent reference during 720 h autoregressive WTD prediction in the UBRB during WY2021. Panels (a–l) show the 12 independently initialized, non-overlapping test segments. Both models used the same WY2019–WY2020 training period, prescribed PME forcing, static attributes, 12 h target pressure-head sequences, and training-period standardization statistics. Their forecasts were evaluated over the same 720 h periods. PredFormer was initialized using the complete preceding 12 h reference pressure-head sequence and generated 12 h pressure-head blocks, whereas PredRNN was initialized using the final pressure-head field from the same reference period and generated pressure-head fields sequentially at hourly intervals. No reference pressure-head states were reintroduced after initialization. Each curve shows the spatial mean absolute WTD error at each forecast hour. The horizontal axis shows simulation time in hours.

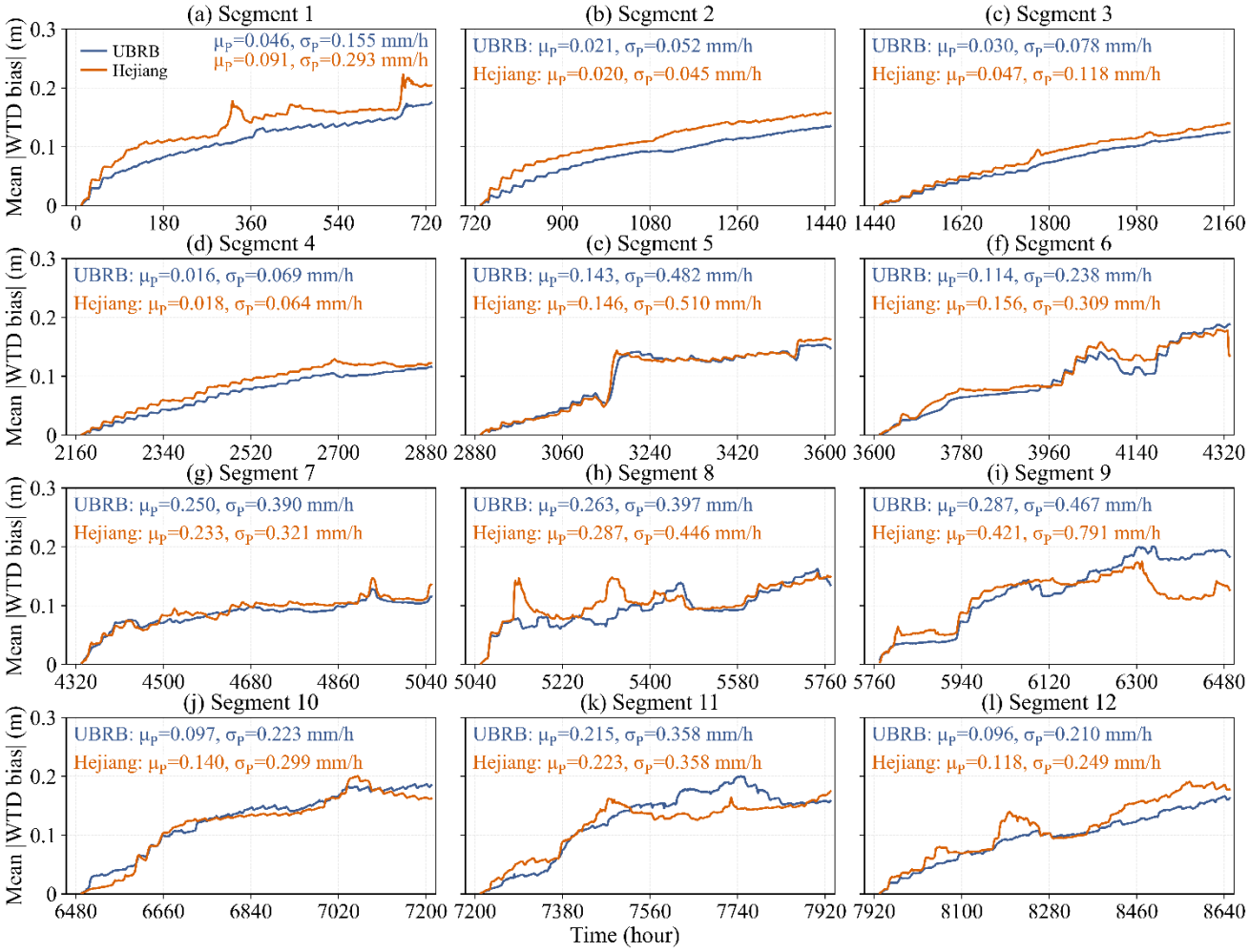


Figure S5. Segment-wise zero-shot cross-basin performance of the UBRB-trained PredFormer in Hejiang during WY2021. Panels (a–l) show the 12 temporally aligned, independently initialized, non-overlapping 720 h test segments. Blue and orange curves represent the spatial mean absolute WTD errors in the UBRB and Hejiang, respectively. Blue and orange annotations report the mean (μ_P) and standard deviation (σ_P) of domain-mean hourly precipitation in the UBRB and Hejiang, respectively, calculated over each 720 h segment. The model used the complete Press. + PME + Static input combination and Post-TS Cross-Attention and was trained exclusively on the unperturbed UBRB WY2019–WY2020 simulations. Its final-epoch checkpoint and UBRB training-period standardization statistics were retained without target-basin training, fine-tuning, or recalculation using Hejiang data. Each segment was initialized using the immediately preceding 12 h of ParFlow-CLM reference pressure-head fields from the corresponding basin, with that basin's prescribed PME forcing and static attributes supplied during rollout. The horizontal axis shows simulation time in hours.

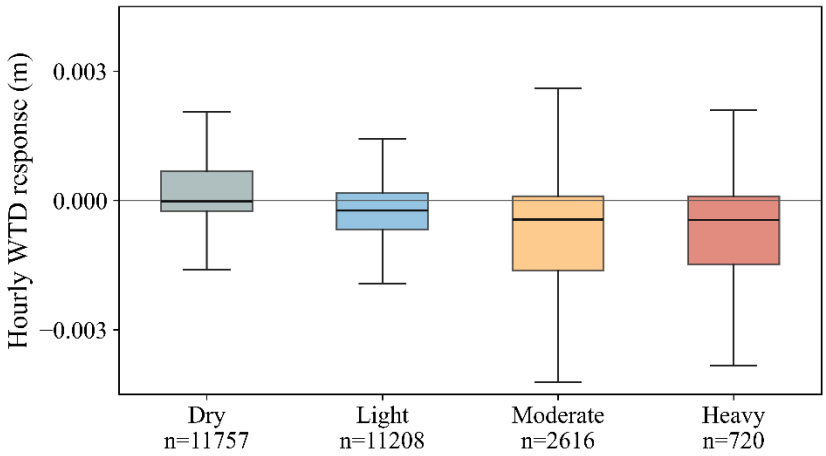


Figure S6. Hourly changes in domain-mean WTD across precipitation regimes in the unperturbed UBRB ParFlow-CLM simulations. Hourly WTD change was calculated as $\Delta WTD_t = WTD_t - WTD_{t-1}$ using outputs from WY2019–WY2021, where WTD_t denotes domain-mean water table depth at hour t. Negative values indicate a rising water table, whereas positive values indicate a falling water table. Each hourly change was assigned to the precipitation regime of its corresponding consecutive, non-overlapping 24 h window. Regimes were classified using 24 h domain-mean accumulated precipitation (P_{24}): Dry ($P_{24} < 1$ mm), Light ($1 \le P_{24} < 10$ mm), Moderate ($10 \le P_{24} < 25$ mm), and Heavy ($P_{24} \ge 25$ mm). Boxes show the interquartile range, center lines show the median. The horizontal gray line marks zero change. The sample size n denotes the number of hourly changes in each regime.

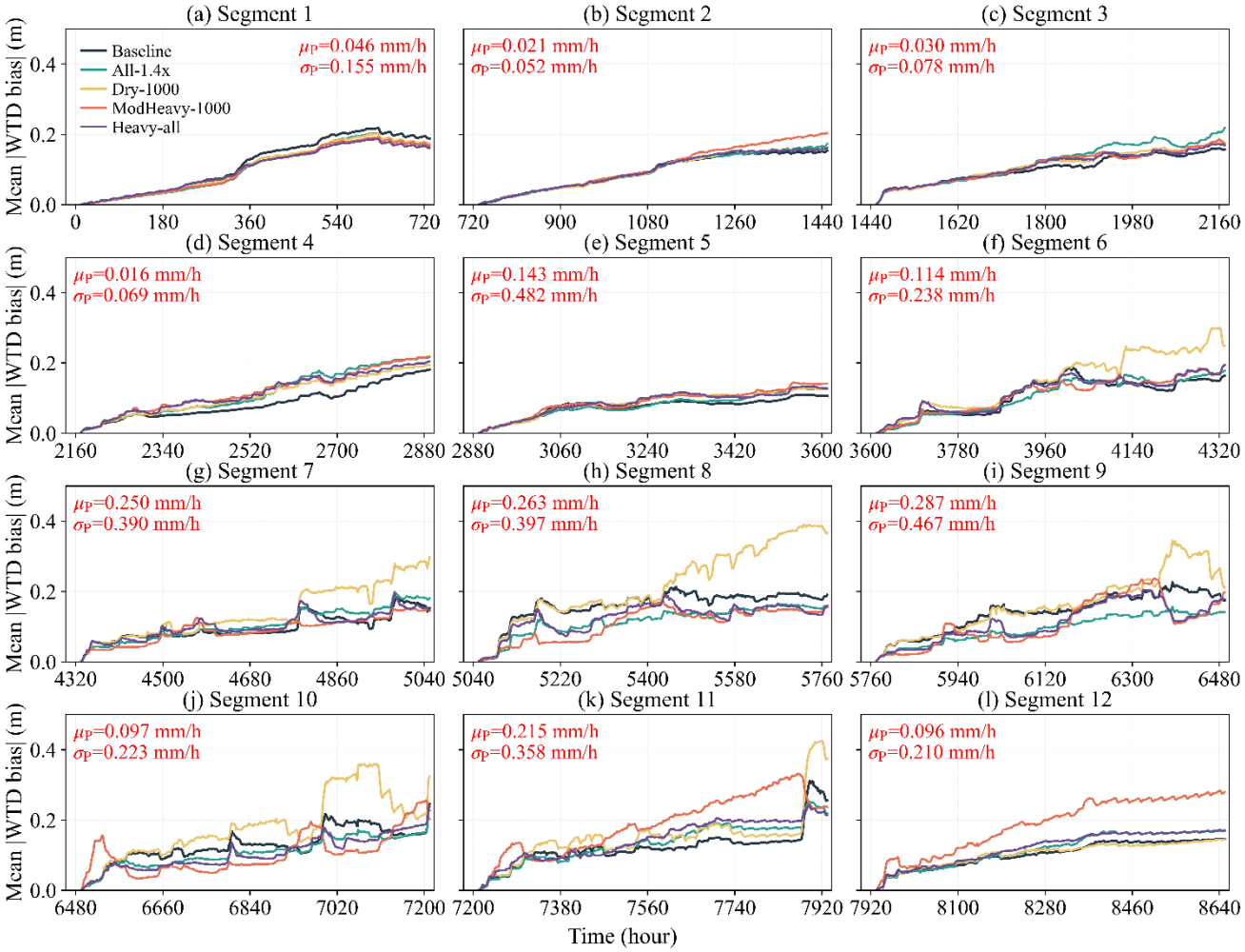


Figure S7. Segment-wise effects of precipitation-regime data augmentation on 720 h autoregressive WTD prediction in the UBRB during WY2019. Panels (a–l) show the 12 independently initialized, non-overlapping test segments. Curves compare Baseline, All-1.4×, Dry-1000, ModHeavy-1000, and Heavy-all. The baseline model was trained using the unperturbed UBRB WY2020–WY2021 ParFlow-CLM simulations, whereas the augmented models additionally used samples from precipitation-perturbed UBRB WY2020–WY2021 simulations. No WY2019 samples were used for training. Each segment followed the same 12 h initialization and blockwise autoregressive rollout procedure. Each curve shows the spatial mean absolute WTD error at each forecast hour. Red annotations report the mean (μ_P) and standard deviation (σ_P) of domain-mean hourly precipitation within each 720 h segment. The horizontal axis shows simulation time in hours. The augmentation strategies are defined in Table 2.